UCID- 18642

THE EXPERIMENTAL TEST ACCELERATOR: DESCRIPTION AND RESULTS OF INITIAL EXPERIMENTS

T. Fessenden, D. Birx, R. Briggs, H. Cavagnolo
J. Clark, E. Cook, G. Craig, C. Hanson,
R. Hester, E. Lauer, E. Moore, V. Neil,
A. Paul (LBL), L. Reginato, D. Rogers, Jr.,
R. Spoerlein, D. Trimble

June 2, 1980

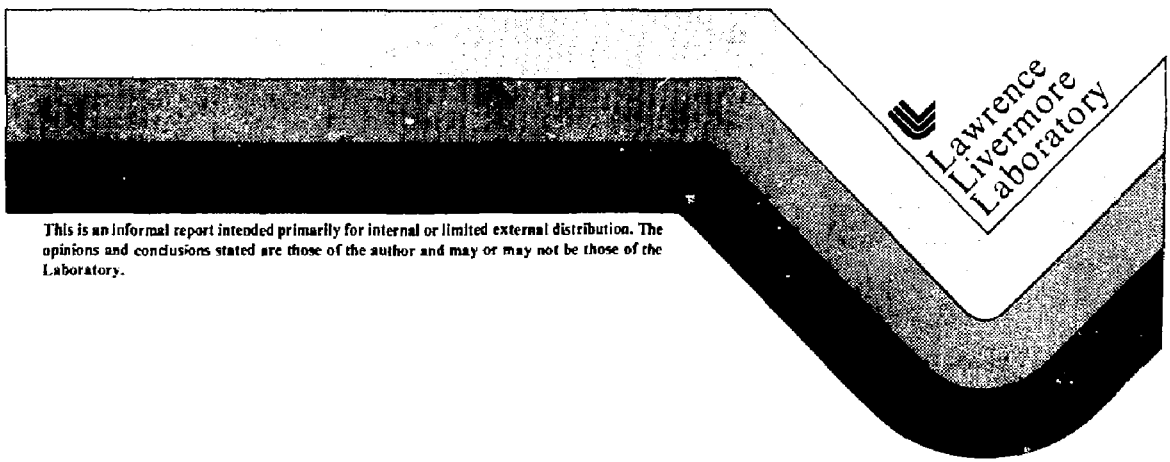

Index

1. INTRODUCTION

The Experimental Test Accelerator (ETA) is an induction accelerator of electrons operating from the same principles as the Astron machine pioneered by Christofilos[1] and others constructed at Livermore in 1963. An improved version of the Astron accelerator operating at 4 MeV was completed in 1968 and extended to 6 MeV in 1970. The peak Astron parameters achieved were 850 Amps, 6 MeV, 300 nsec pulse width, and an average rate of 5 pulses per second. Normally this machine ran at 400 Amps and 2 pps. Like ETA the Astron machine had a burst capability of as many as 20 pulses separated by 1.2 msec. The ETA is similar to the ERA accelerator[2] developed at Berkeley in 1971 in appearance and pulse shape. The principal difference is the higher current of the ETA and the provision for a rapid pulsing burst mode.

The design parameters of the ETA are 10,000 Amps, 5 MeV, 30 nsec pulse width with a burst capability of 5 pulses separated by one millisecond. The machine is capable of one burst every second or it can be run at the continuous rate of 2 pulses per second. When operating properly, the ETA shows excellent reproducibility from pulse-to-pulse. Our diagnostics use 7000 series Tektronix oscilloscopes triggered externally. Even at 10 nsec/division sweep speeds, successive voltage or beam current pulses are usually indistinguishable on photographs of the oscilloscope traces.

As much of the Astron accelerator as possible was used to construct the ETA. The X-ray shield for both accelerators is composed of the same concrete blocks. Initially, almost all of the vacuum pumps and valves were orignally part of the Astron vacuum system. The high power vacuum tube modulators that were used with Astron are used with ETA. Even the thyratrons used with Astron

are used as primary switches in the circuits that charge the ETA Blumleins. This "borrowing" resulted in a considerable cost saving in the construction of ETA at the expense of some initial problems with system reliablity.

Initial testing of the ETA injector began on November 11, 1978 and continued through March 1979. During this period beams of 5 kA at 2.2 MeV were generated and delivered to the exit of the gun. The 10 accelerator units that constitute the remainder of the ETA were installed in April and May and testing of the complete accelerator began in June 1979.

In October we experimented with beams at the accelerator output at currents up to 6.5 kAmps and 4 MeV in a single pulse mode. This is nearly 10 times the current ever accelerated by the Astron machine. During this month alone more than 150,000 pulses were put on the machine at the rate of 0.5 pps.

The final installation of the electronics necessary to provide a five pulse burst capability was completed in February 1980. The earthquake that jolted the Livermore area in late January caused considerable mechanical damage to the ETA, particularly the anode, and delayed further beam experiments until April. While the earthquake damage was being repaired, the 5 pulse burst electronics were completely checked out at 70% of the design voltage.

At this time we estimate that over 1.1 million pulses have been put on the injector with nearly 450,000 pulses on the accelerator units. Most of this running has been at an average rate of one pulse/second. A prime function of the ETA is to develop accelerator technology so that larger more powerful high current linacs can be constructed with as little risk as possible. Accordingly, these tests have revealed several technological weak points in our original ideas or how to build a high current linac. The large 10 inch diameter oxide cathodes have continuously shown evidence of poisoning and,

although 10 kAmp cathode emission in ETA has been achieved, to date these cathodes have operated reliably at only 6-8 kAmps. The use of extremely short trigger pulses required more trigger amplitude than anticipated which caused breakdowns in the trigger cables. A glue joint in a plastic interface that must withstand the high pressure of the spark gap gas was shown to be inadequate etc. Many of these problems and their resolutions are described in detail in section 7.

Although the above difficulties have as yet prevented our obtaining the full design parameters of the ETA, machine operation at about 65% of the design current and 80-90% of the design voltage has been obtained and the beam transport is in full accord with the physics design. As anticipated theoretically and shown experimentally, the gun must be operated at voltages near or above 2.5 MV to produce a 10 kAmp beam. Operation at too low a gun voltage results in the formation of a virtual cathode in the gun that destroys the beam emittance resulting in beam spill in the accelerator. Theory and experiments have shown that beams at currents up to 5 kAmps can be transported through the accelerator units with or without energizing these units. (Theory indicates no problems in transporting beams at 10 kAmps and above through the ETA transport.)

As yet no clear evidence exists for the presence of unstable accelerator modes. However, modes do exist that may disrupt the beam in ATA and not be important in ETA because of its shorter length. Consequentaly, r.f. experiments aimed at elucidating the potentially important instabilities of high-current electron linacs will receive high priority in future ETA experiments.

This report does not contain information on the development of several key components of the accelerator that have already been published. A description of the spark gap Blumlein switch and its developmental tests is contained in

reference 3. Reference 4 presents the development of the transformer used to charge the Blumlein. Tests of the ferrite cores used in the ETA are described in reference 5. The ETA gun and associated pulse power system is also described in reference 6.

This report does cover a description of the system and diagnostics, a comparison of design codes with experiments on beam transport, and the experience in several special problem areas. Section 2 of this report contains a mechanical, and section 3 an electrical description of the accelerator. Section 4 describes the ETA diagnostic system and section 5 contains some of the more relevant pulse power tests and measured waveforms of the machine. A description of the operation including both theory and experiments is presented in Section 6. Comments on some of the special problems and their status are contained in Section 7.

2. ETA MECHANICAL DESCRIPTION

The ETA has two major sections; a 2.5 MeV 10 kA electron gun and a 2.0 MeV 10 kA accelerator assembled from eight 250 keV accelerating cells. The complete system is designed to produced a 40 ns 4.5 MeV 10 kA electron beam pulse. The system can operate in a single pulse mode at up to two pulses per second and in a burst mode of five pulses at up to 1 kHz with a maximum time average of five pps. The system uses a nearly continuous solenoidal magnetic transport. A cut-away sketch of the ETA showing the location and orientation of the components of the machine is shown in Figure 1.

2.1 ELECTRON GUN

The electron gun (Figure 2) has five major subassemblies - three housing sections, the cathode/grid assembly and the anode assembly. The three housing sections bolt together to form a cylindrical tank with re-entrant ends. Each end has a mounting flange for either the cathode/grid assembly or the anode assembly.

There are five induction units in both end sections of the tank. The induction units have oil-immersed toroidal ferrite cores and operate in series to produce a 1.25 MV potential across a ceramic accelerating column. The ceramic column is the interface between the oil dielectric in the induction units and the high vacuum in the accelerating region. The center spool supports the high voltage electrode and vacuum pumping manifolds.

The cathode grid assembly consists of the cathode, a wire mesh grid, the grid induction unit and a bucking coil. The cathode is a 25 cm diameter oxide button operated at 850-950°C. The hot oxide cathode was selected as a consistent electron source at high repetition rates. The bucking coil is used to counteract any axial magnetic field at the cathode face.

The anode is a hollow re-enterant structure. The inner bore tapers from 25 cm diameter to 15 cm diameter at the beam exit. The beam size through the transition is controlled by magnet coils wrapped around the inner tube of the anode.

2.2 ACCELERATOR

The accelerator consists of 8 (originally 10) units each of which adds 250 kV to the beam energy. Each unit is driven on each side by a transmission line coupled to a Blumlein pulse source. On the top and bottom of the units are resistive loads that parallel the accelerating gap and limit the voltage across the accelerator. The accelerator units are paired in that two Blumlein pulses drive two accelerator units. This was done to improve the drive symmetry to the accelerators.

The eight accelerating cells (Figure 3) are induction units with toroidal ferrite cores. The 250 kV accelerating field is produced across a one inch gap. The ferrite cores are oil submerged and a ceramic insulator is used as an oil/vacuum barrier. The two pulse power lines into the cell are azimuthally symmetric to eliminate possible transverse magnetic fields. The cell contains a magnet coil to maintain continuity of the solenoidal beam transport. The beam tube sections between accelerating cells include vacuum pumping ports, beam position and current monitors, and vacuum gauges. These tubes are surrounded with transport magnet coils.

2.3 BLUMLEIN PULSE FORMING NETWORKS

The 250 kV pulses that drive the ETA are obtained from Blumlein pulse forming networks. These use low conductivity water as a dielectric and have an electrical "length" of 40 nsec on the gun and 48 nsec on the accelerator. Each of 10 gaps in the gun is driven by two Blumleins to produce the necessary

2.5 MV. With the three trigger Blumleins and the grid-drive Blumlein, there are a total of 24 Blumleins mounted on the gun. The accelerator uses 8 Blumleins and one trigger Blumlein. The spark gaps that discharge all of the Blumleins are filled with a mix of N_2 with 8% SF_6 and circulated by three 250 H.P. turbine blowers.

2.4 AUXILIARY SUPPORT SYSTEMS

The ETA has several auxiliary support systems that can be described briefly. Ten cryogenic pumps maintain a system pressure of $1 \times 10^{-6} - 5 \times 10^{-6}$ torr in the accelerating and transport sections. An ion-exchange polishing system is used to supply 18 MΩ-cm de-ionized water to the Blumleins. An oil filtration and degasification system circulate oil through the gun and accelerator induction units. A low conductivity water system provides cooling water for the focusing magnets, resonant transformers and anode tubes.

3. POWER CONDITIONING SYSTEM

The power conditioning diagram for the 2.5 MeV ETA gun is shown in Fig. 4. The primary power system must supply the beam energy as well as the intentional losses in the compensation network, ferrite, and switching system. Past experience has shown that in order to achieve a stable and repeatable beam pulse, a 0.1% or better regulation is necessary from the pulse power system. The high degeee of regulation is provided by a hard tube modulator in series with the main charging supply. The modulator tailors the charging voltage to the primary capacitors which deliver the burst energy. These capacitors are sequentially discharged at the desired rep-rate by a thyratron switch into a ten-to-one, step-up transformer that resonantly charges the Blumlein. The Blumlein energy is delivered to the ten series ferrite loaded cavities by means of a coaxial air blown sparkgap.

3.1 MODULATOR AND POWER SUPPLY

With an output requirement of 22 kV and allowing a tube drop of 5 kV, the power supply would have to be operated at a minimum of 27 kV. To supply the full voltage at 57.8 A would have meant a costly modification to the power system utilized for the Astron accelerator. A compromise was reached where the ratio of peak-to-average power requirements were satisfied by enlarging both the energy storage and power input. By rearranging the configuration of the Astron capacitor bank, we were able to obtain a total of 1770 μF at 40 kV. The voltage sag when operating in the burst mode is about 7 kV.

The regulated voltage to the pulse forming capacitors is generated by five hard tube modulators operated as constant current devices. The basic modulator is the same as for the Astron accelerator except that the WX4852

output tube delivers constant current by calling for a linear voltage ramp into the capacitors. Five such modulators provide an overall charging current of 25 A to a total of 578 F over a .5 sec charge time.

3.2 SWITCH CHASSIS, RESONANT TRANSFORMER AND BLUMLEIN

The accelerating potential of 250 kV at 50 ns duration is delivered from a Blumlein by a shorting switch (spark gap). The pulse conditioning components are shown in Fig. 5. They consist of a 3 μF capacitor discharged by a dual FX 2508 thyratron into the primary of a step-up transformer which charges the Blumlein.

The Blumlein is a 10 Ω water line. This impedance is determined by the load requirements: 20 kA total drive at 250 kV. The choice of water as the dielectric permits the construction of high energy density networks. Water has the added advantage of being able to recover from a breakdown without having formed conducting by-products. However, water does require a circulation system to remove dissolved gases and conducting ions. The breakdown strength of water is a weak function of the time the voltage has to be held off. By selecting a 15" outer diameter pipe the voltage gradients were limited to 100 kV/cm.

All surfaces at the high gradient points are radiused and electropolished to remove whiskers and protrusions. All Blumlein components are constructed of stainless steel which is less likely to suffer surface damage in the event of a breakdown.

The design of a charging transformer for the Blumlein is influenced by the load, switch, step-up, and charge time. The load is the Blumlein capacitance, about 10 nF. The switch for the transformer is a FX2508 thyratron capable of 6 kA peak current at 25 kV. The use of this thyratron imposed a further constraint for a non-reversing current unless costly auxiliary circuits such as diodes were utilized. Based upon the thyratron

capabilities and limitations, the transformer is required to have a minimum step-up of ten-to-one and a non-reversing current of 10 kA. The 10 kA required use of two parallel thyratrons operating at 5 kA, for which ample testing in the millions of shots existed.

Since the load is capacitive, a resonant charging transformer was logical. The most commonly used transformer of this type has a coefficient of coupling K = .6. This yields energy transfer efficiencies over 90%. Unfortunately, this requires a bi-directional switch. After a thorough circuit analysis, computer generated curves showed that a particular set of transformer parameters did indeed satisfy all the requirements. The voltage and current waveforms in Fig. 6 correspond to a coupling coefficient K = 0.525 and a ratio of primary to secondary frequency ratio of 0.69. The waveforms show that the current in the primary is non-reversing and near zero at the secondary voltage peak. The primary voltage has actually reversed 60% of this time, but this energy remains in the capacitor since the thyratron opens at the zero current point. Although this case is not optimum from an energy transfer standpoint, the remaining energy has no adverse effects on the spark gap recovery time and does satisfy the step-up and primary current requirements. The final transformer consisted of a 7-1/2 turn primary wound on the outside of 150 turn secondary. The 7 mil, 2" wide capacitor grade aluminum foil was insulated by 6" wide, 7 mil mylar with .5 mil Kraft paper (for oil wicking). A cross section of the final transformer is shown in Fig. 7. Other components in the transformer consist of mid-potential biasing for the trigger electrode, coupling capacitor for the trigger, varistors damping and decoupling inductor for high frequencies.

3.3 SPARK GAP DESIGN

A cross section of the coaxial spark gap is illustrated in Fig. 8. The spark gap bolts on to the lower end of the Blumlein line and switches (shorts) the mid conductor to ground. The coaxial cylindrical geometry was adopted for

two main reasons--long life and high rep-rate. The trigger electrode is expected to wear uniformly in the axial direction with no change in the electrical characteristics resulting in tens of millions of shots before replacement. The coaxial geometry further assures high gas velocities and low pressure drop to achieve the 1 kHz burst rate. The chamber on the outside of the spark gap reduces the pressure drop and allows uniform gas flow. The interface insulators were made of polycarbonate resin because of their strength and resistance to high voltage tracking. The trigger electrode and sparking area for anode and cathode are made of tantalum for easy replacement after wear.

The development tests showed that a 1 kHz burst rate could be achieved with a mixture of 6-8% SF_6 and Nitrogen flowing at about 4 cm/ms. The gauge pressure for full voltage operation was about 100 psi. With the spark gap running at about 75% of self break, the jitter was in the few nanosecond range and the rise time was 12 ns.

3.4 FERRITE CORES

The total 2.5 MeV gun voltage is obtained by stacking ten accelerating cavities (250 kV each) in tandem. Because of the re-entrant structure of the gun, the ferrite cores had to be manufactured in twelve segments glued in pairs to form a toroid .96 m I.D. and 1.28 m O.D. The gap at the joints was less than .04 mm. The ferrite segments were PE11B supplied by TDK. Eight such segments maintain the required 250 kV for 50 ns on the accelerating gap. The total flux swing from this ferrite is about 5 kG with a coercive force of about .25 Oersted. The ferrites are immersed in oil which is outgassed and filtered.

4. ETA DIAGNOSTIC SYSTEMS

The ETA accelerator has a standard set of diagnostics that tell the status of the vacuum in various areas, pressure in various parts of the system, etc. This section is devoted to diagnostics developed especially for the ETA accelerator.

4.1 PULSE POWER MONITORING

Pulsed voltages in various sections of the accelerator are measured with the aid of a capacitor voltage probe. A sketch of this probe is presented in Figure 9. This probe has a risetime faster than our oscilloscopes and "droops" at a rate determined by the load on the probe. For fast pulse applications this time is adjusted to 1.5 μsec. This gives a sensitivity into 50Ω of from 10^4 to 10^5 volts/volt depending on whether the probe is installed in water or oil. The probe consists of a capacitor formed by painting a conducting epoxy coating over a parylene insulator as shown in Fig. 9. This forms approximately a 1 nF capacitor which is connected via a resistor ($\approx$ 1.5 kΩ) to a coaxial line and patched into the control room.

Capacitor probes are used to measure the output voltage of each of the 35 Blumleins on the ETA accelerator. The outputs of those Blumleins that drive the gun is measured in the gun across the 10 gun gaps. For the accelerator the voltage is measured across the accelerating gap. Capacator probes are also used to measure the Blumlein charge voltage on each Blumlein. In this application a passive compensation at the oscilloscope is used to extend the droop time to 150 μsec. More than 70 probes are used on the machine. Figure 10 shows a diagram of the system for switching these probes to two oscilloscopes. A single control selects which Blumlein charge and output pulse voltages are connected to the oscilloscope. A pair of switches exists for the gun and the accelerator.

The capacitor probes that monitor the voltage across the gun are coupled through the selector switch to a summing amplifier whose output is coupled to an oscilloscope in the control room. In this way the total output voltage of the gun is measured. A similar system exists for the voltages across the accelerator cavities.

The ability to make jitter measurements on every spark gap to within one nanosecond is a third feature of this system. The gun or accelerator voltage pulse selected by the 30 channel switch is also patched to a digital counter. This is then used to measure the firing time delays between the master trigger and any sparkgap.

4.2 BEAM MONITORING

The current emitted by the cathode is measured by a resistive shunt in the cathode assembly. A capacitor probe is used to measure the grid voltage. This is located just behind the vacuum-oil interface approximately 3 ns from the cathode plane.

The beam in the accelerator is measured by a resistive wall current monitor. These are located at the gun output, in the center of the accelerator, and at the acceleration output. These monitors employ a 12.7μm thick stainless steel foil resistor that encircles the beam tube. The voltage developed by the beam image current passing through the resistor is measured at four positions around the circumference of the beam tube. These voltages are used to determine the beam current as well as the location of the beam centroid in the pipe. These devices have a rise time less than one nanosecond with a sensitivity of 1000 A/volt.

4.3 ENERGY ANALYZER

The energy analyzer[7] used with the Astron accelerator has been modified for use with the ETA. New detectors were purchased in order to increase the frequency response of the system.

4.4 BEAM SIZE AND EMITTANCE MEASUREMENTS

Measurements of the beam size and emittance are made with the device that stops the beam. After acceleration, ≈95% of the beam stops on a water-cooled carbon plate. A pattern consisting of several hundred thin slots cut in the carbon plate forms many retangular "beamlets" of the current that passes through the plate. After drifting about 20 cm, these are allowed to pass through a .25 mm aluminum plate--the back of which is covered with a fast phosphor with a light decay time constant of approximately 0.5 ns. A closed circuit television system is used to scan the image produced by the rectangular beamlets. A gateable intensifier with a minimum window of 5 ns is located in front of the television camera.

The beam size is obtained by measuring the number of rectangular beamlets on the television monitor. The beam divergence is obtained by measuring the width of the rectangular beamlets and subtracting the known width of the rectanguiar slots. If the beam "tune" is adjusted so that a beam antiwaist exists at the plane of the carbon stop, the beam emittance is obtained from the product of the beam area and angular divergence.

This system is capable of measuring the beam size and emittance over times as short as 5 ns. As a consequence the evolution of the beam during the pulse can be studied.

When gas propagation experiments are in progress, this system will also be used as removable beam dump. In preparation for experiments the beam stop will be inserted and final tuning adjustments made. The beam stop will then be remotely removed allowing the beam to pass into the experimental gas cell.

5. PULSE POWER TESTING AND MACHINE COMPENSATION

This section contains the checkout and testing of the most relevant components of the accelerator. In particular section 5.1 contains tests and characteristics of the Spark gaps used throughout the machine. Section 5.2 contains measurements and computor modeling of the voltage that accelerates the beam in the gun. Section 5.3 presents measurements and analyses of the voltage that appears across each accelerator unit and Section 5.4 contains a discussion of the grid drive circuit.

5.1 JITTER TESTS OF THE ETA SPARK GAPS

This section contains tests of the ETA spark gaps and analyses of the voltages used to accelerate the ETA beam.

ETA contains 35 high gas pressure spark gap switches, 34 of which should fire at as nearly reproducible time delays as possible (see Fig. 11). There are two separate mechanisms which contribute to the distribution of firing time delays of a system consisting of many spark gap switches.

1. Identical spark gaps which should have equal mean times have a random distribution of firing time delays. Several comments follow about this width of the firing time delay distribution of a single gap with fixed parameters.

   a. Under optimum conditions, the width for the ETA gap is impressively good, (only 2 or 3 ns)--see Figs. 12 and 13.

   b. The narrowest widths measured on ETA gaps are significantly better than those for the ETA test gap.[8] We attribute this difference to the fact that the ETA trigger pulses have a faster rise time and a larger amplitude than the test gap trigger pulse. The switched Blumlein triggers on ETA produce pulses with a 20 ns rise time and 80 kV amplitude, which voltage doubles to 160 kV. The test

gap trigger transformer produces pulses with 80 kV amplitude and 100 ns rise time. In this case the voltage at the open end of the trigger cable does not double because the cable is too short.

c. There is evidence that the jitter of the ETA gaps would be improved for some sets of parameters if the trigger pulses had a still larger amplitude or a longer time duration. Under optimum conditions, the time delay from the head of the trigger pulse until main gap fire is about 50 ns. Most of this delay is the time for the trigger gap to breakdown--the additional delay until main gap fire is only 1 or 2 ns.

2. The mean time delay is a function of the parameters (main gap voltage, trigger pulse amplitude, gas density and composition, and gap geometry). In general, the time delay decreases with increasing gap voltage, increasing trigger pulse amplitude and decreasing gas density. With the test gap,[8] significant variations of the mean time were sometimes found when we attempted to repeat measurements with identical parameters in tests separated by many firings. On ETA under optimum conditions, the 20 gun gaps have a 15 ns distribution of mean times.

All of the time delay distributions are measured with a quartz oscillator controlled timer which is started by the trigger pulse and stopped by the firing pulse. The timer has 0.1 ns resolution and records to the nearest 1 ns.

Figure 12 shows a typical variation of mean time delay and jitter obtained at three charge voltages and gas pressures. Note that as the firing delay exceeds the trigger pulse width, the jitter worsens. Figure 13 shows optimized distributions for a trigger Blumlein and for a gun-drive Blumlein cascaded. These data show that cascading the trigger and drive Blumleins does not contribute significantly to the jitter.

Figure 14 shows data obtained at 20 psig with the Blumlein charged to 20 kV. This data shows the time for the triggered gap to close (+) and the time for the spark gap to close (x) as a function of the amplitude of the trigger pulse. At large trigger voltages, the sparkgap closes within 5 nsec of the closure of the triggered gap. As the voltage is lowered, the closure time for both gaps lengthens until they both became approximately equal to the pulse width. The gap could not be fired at lower trigger voltages.

The time duration of the ETA trigger pulses is about 50 ns. If the trigger pulse ends before the trigger gap breaks down, the jitter is much worse than if the trigger gap breaks down while the trigger voltage is still up.

5.2 ETA GUN WAVEFORMS AND COMPENSATION

Experiments have shown that the ETA gun voltage pulse resembles a half-sine wave with an amplitude at half-maximum of approximately 40 nsec (see Fig. 17). This waveform results because: A) The inductance of the sparkgap limits the rise time (e-folding) of each Blumlein output pulse to $\approx$10 nsec; and B) Small differences in the firing time delays between the 20 gun Blumleins further slow the voltage risetime and broaden the pulse.

A simple electrical model of the gun containing the most important circuit elements is shown in Figure 15.

The ETA Blumleins do not generate square pulses principally because of the inductance of the closing switch and because the inner and outer coaxial lines that form the Blumlein pulse forming network are not of equal electrical length. The rise time τ of the output pulse is given by the switch inductance divided by the characteristic impedance of the outer line of the

Blumlein. If τ_1 is twice the transit time of the inner coax and τ_2 is twice the transient time of the outer coax, Briggs[9] shows that the output voltage waveform is given by

$$V_s/V_{charge} = 2(1-\exp(-t/\tau))\, U_1(t) - (1-\exp(-t_1/\tau))\, U_1(t_1) - (1-\exp(-t_2/\tau)) - 2\, t_2/\tau \exp(-t_2/\tau)\quad U_1(t_2) \qquad (1)$$

with $t_1 = t-\tau_1$, $t_2 = t-\tau_2$, and $U_1(t)$ is the unit step function. For the ETA gun Blumleins τ = 10 nsec, τ_1 = 40ns, τ_2 = 46 nsec.

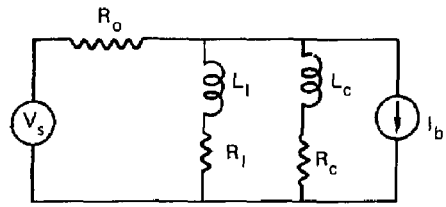

Fig. 15

Simplified Model of ETA Gun

The equivalent output impedance (R_o) of the source voltage in figure 15 is 53 Ω. The circuit is loaded by the grading resistors along the insulating column of the gun. These have an estimated inductance (L_I) of 300 Ω and a resistance (R_I) of 250 Ω. In parallel with these is the compensation circuits which are shown as a series resistance (R_c) and inductance (L_c). The beam load is modeled as a current source as shown.

The voltage V_A will have a faster risetime than the source voltage due to the inductors L_c and L_I. In order to avoid overshoot[10] the time constants of these circuits should be adjusted to equal the rise time τ of the source voltage V_s. In this limit analysis shows that the voltage V_s will rise with a time constant reduced by the factor $1 + R_o/R_{c\|}\, R_I$. However, the Blumlein charge voltage necessary to generate the 2.5 MV at the ETA anode will be increased by the same factor. Figure 16 shows the Blumlein charge voltage necessary to produce 2.5 MV across the grid-anode gap with and without beam as a function of the values of the compensation resistors for the parameters of the ETA gun. Also shown is the relative improvement in pulse risetime as the value of the compensation resistor is varied.

The compensation circuits presently installed in the gun consist of a 36Ω resistor in series with a 360 nH inductor in each of 20 compensation cans located on the top and bottom of the gun. Thus across each gap the equivalent circuit is 18 Ω in series with 180 nH. By removing all the circuits from the top cans (a relatively easy chore), the equivalent resistance and inductance can be doubled. These points are indicated in Figure 16.

Testing has shown that, although the jitter in firing of all the ETA spark gaps is usually less than 3 ns, the 20 gun sparkgaps fire at times that differ by up to 20 ns as discussed in Section 5.1. This situation was modeled using the "Septre" circuit-solving computer code available on the LLL computer system. The voltage drive for each gun gap was that given by Eq. (1). However, the time at which each gap voltage was applied was taken from experimental measurements. The model includes the ferrite inductance L_f, the gap capacitance C_g of all 10 gun gaps. The gun model contains the compensating circuits on each end of the gun and the resistance (R_I) and inductance (L_I) of the resistor that grades three large ceramic insulators of the gun. Because of the size of the gun, the transit time of a wave from

one end of the gun to the other is approximately 20 nsec. Also the time for a wave to travel around the gun circumference is about 6 ns. Waves of this nature can not be studied with this model. Only the shunt capacitors between the gun gaps and the inner cylindrical shell of the gun were retained. Other models in which the finite size of the gun was modeled by an L-C transmission line showed the need for the gun compensation circuits.

Figure 17a shows the experimental voltage waveform obtained by electronically summing the voltages across all 10 gun gaps. Figure 17b shows a normalized voltage waveform obtained with the aid of the "Septre" computer code using the experimentally obtained firing times listed in the figure caption. Figure 17c shows the normalized gun waveform that the computer predicts is obtainable if all 20 gun Blumleins could be fired simultaneously. As can be seen the computor model that includes variations in turn-on times of the different voltage sources produces waveforms practically indistinguishable form the experimental waveforms.

The reason for the relatively large differences in firing times of the sparkgaps is not completely understood. Experiments have shown that a typical sparkgap requires 40-60 nsec to close after being triggered. Variations in firing time can result from: variations in the alignment of the sparkgap electrodes; small differences in the values of the resistors used to bias the trigger electrode; variations in sparkgap electrodes resulting from spark erosion; or blown trigger cables. Further experiments are needed to sort out this issue.

5.3 ETA ACCELERATOR WAVEFORMS AND COMPENSATION

At present, the compensation for ETA accelerator cavities consists of resistive loading only, with the resistor value determining the cavity gap voltage. The equivalent circuit is

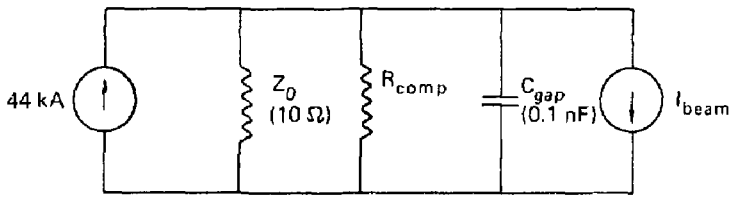

Figure 18

Equivalent Circuit of an ETA Accelerator

We need 250 kV (gap voltage) for 220 kV Blumlein charge voltage. The ferrite inductance is large enough that for the pulse duration only slight voltage droop will occur. The gap capacitance effects only the voltage risetime (RC time constant is in the ~ 1.0 ns regime). For the purpose of determining the acceleration voltage effects of both may be ignored. The output voltage is then defined by the source voltage and impedance, the value of the compensation resistance and the amplitude waveshape of the beam current. With the beam present, 34 kA drives the parallel impedances. With the required gap voltage = 250 kV one obtains $R_{comp} = 28\,\Omega$. Note that if the beam is not present the voltage across the cavity is 323 kV.

This analysis does not consider that the Blumlein output voltage pulse duration is longer than the beam current duration. Experimental data show the beam current to have a risetime of ~ 5 ns and a full-width half-max of ~ 30 ns while the acceleration voltage FWHM is 50 ns with a risetime of 10 ns. Depending on the relative timing of the two pulses the gap voltage will be of the form:

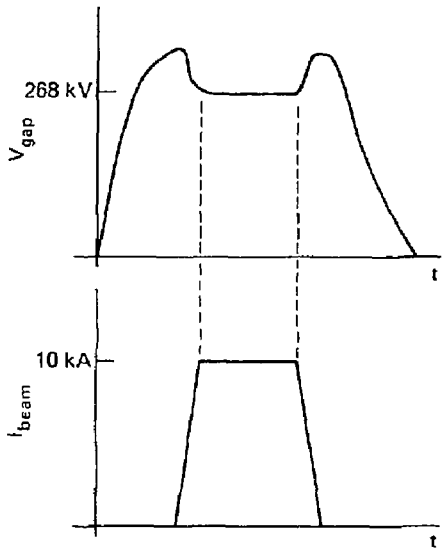

Fig. 19 Sketch of Expected Waveforms of Accelerator voltage with Beam

The maximum gap voltage (323 kV) appears when there is no beam, otherwise the voltage will peak between 323 and 268 kV as a function of beam arrival.

The gap voltage risetime may be decreased by inductive peaking in the compensation circuit as shown by Ian Smith[10]. Inductive peaking is achieved by adding an inductance in series with the compensation resistor such that

$L/R = t_r = 10$ ns

$L = 375$ nH

However, this has a detrimental effect on the transient response to the beam. As Ian shows, the input voltage risetime will be reduced to 7.9 ns. However, the inductor will induce a transient as the beam current rises (the amplitude of this inductive kick will decrease as beam risetime increases) plus a L/R decay on the constant current portion of the beam.

Figure 20 shows an oscillogram of the voltage across an accelerator unit measured with a 500 mHz band width system. This is the waveform that exists with no beam present. The front porch on this signal results from the feed through of the spark gap trigger pulse. The slight notch is due to reflections in the transmission lines feed to the accelerator cell. The back porch clearly shows the effect of the unequal length Blumleins.

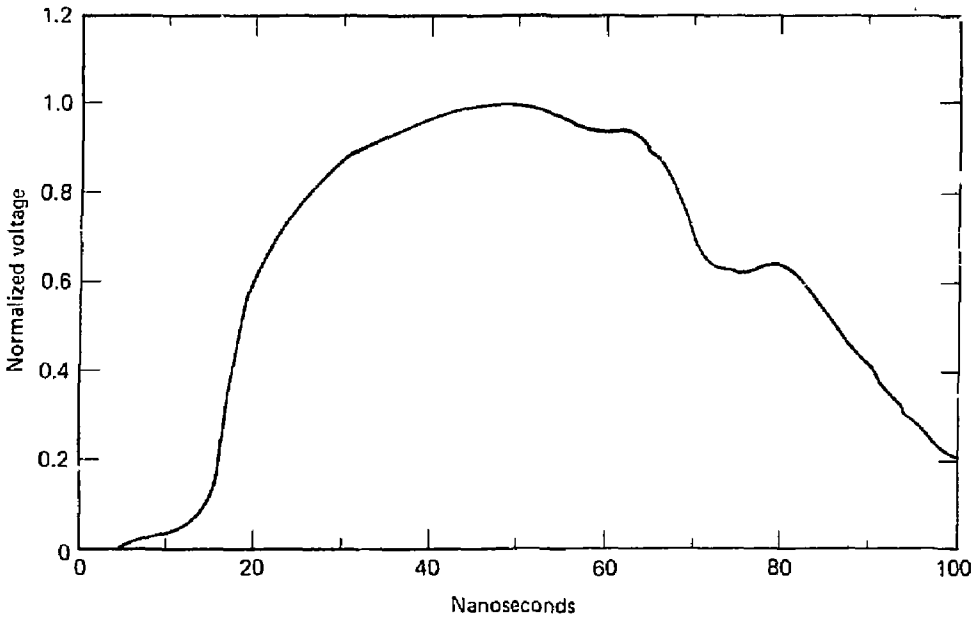

Figure 20

Measured Wave form of Voltage Across an Accelerating Unit.

5.4 GRID VOLTAGE: CIRCUIT AND WAVEFORMS

A grid biased positive with respect to the cathode is used to extract the ETA beam from the oxide cathode. Several grids have been used. Among these are a woven pattern of one mil tungsten wires in approximately a one millimeter mesh, a grid formed of 10 mil tungsten wires in a 5 millimeter

mesh, and a honeycomb structure found of one mil thick stainless ribbon approximately one cm wide in a honeycomb structure of 5 millimeter mesh. The transmission of of electrons through the fine tungsten mesh is approximately 95%. Transmission through the titanium mesh is 90% while the transmission through honeycomb structures is near 70%. The grid is located 1.5 cm in front of the cathode plane. If the cathode emits according to the Child-Langmuir relation, a beam of 11.7 kAmps at a grid voltage of 80 kV will be extracted from the cathode.

This voltage is generated by a standard ETA Blumlein charged to 200 kV. The 200 kV pulse is attenuated by 0.4 and coupled through 8-55 Ω trigger cables to the grid. Care was taken to match the 10.5 Ω output impedance of the Blumlein to the 6.8 Ω of the eight cables in parallel. The circuit is shown in Fig. 21. Notice that the only load on the circuit is the beam itself. If no current is emitted by the cathode (i.e., the cathode is dead), the voltage will double at the cathode to 160 kV. This is near the maximum we can safely place on the cables without breakdown. The attenuator is also matched in the reverse direction in that energy which reflects due to a mismatch at the grid is not reflected at the attenuator. As a consequence waves in this circuit are rapidly damped.

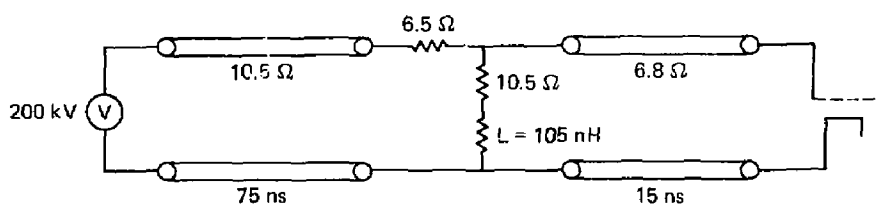

Figure 21

Since the grid voltage originates from a standard Blumlein pulser, its risetime is inductively limited to 10 nsec. The inductance L is used to improve the rise time to approximately 7 nsec as explained in 6.2

The circuit can be analyzed by using the transmission line equations and the Child-Langmuir equation for the relation between the grid voltage (V_g) and the cathode current (I). The results are presented graphically in Fig. 22. In Fig. 22a the expected cathode current is plotted as a function of the voltage pulse (V_+) coupled through the attenuator in the forward direction. This current is shown for several cathodes emitting as fractions of the design Child Langmuir current

$$I_{cL} = 500 \times 2.33 \times 10^{-6} \, V_g^{3/2}/(1.5)^2 \qquad (2)$$

Figure 22b shows the relation between the voltage that appears across the grid-cathode gap and the forward voltage V_+ for the same multiples of the Child-Langmuir current. A match occurs when the forward voltage equals the grid voltage (V_g).

These calculations show that the system should be reasonably well matched at the design values. They are also useful for interpreting the voltages and currents that are observed if the cathode emits as some factor of the Child Langmuir value.

6. BEAM DYNAMICS IN ETA: THEORY AND EXPERIMENT

This section is devoted to discussions of the beam physics of the ETA accelerator. Results of experiments are compared with predictions of two computer codes in order to understand the operation of the machine.

6.1 OPERATION OF THE GUN

In this section we describe theoretical predictions of the characteristics of the ETA gun, and compare these predictions with experimental data. Computational studies of the beam dynamics in the ETA gun were carried out using the computer code EBQ. Some of the work carried out prior to March, 1979 is described in Ref. 11.

6.2 CODE MODEL

The computer code EBQ[11] is a steady-state, azimuthally symmetric, self consistent code. In the design of the gun, the code was used to determine the equilibrium flow of electrons from the cathode, through the extraction grid, across the grid-anode region and into the hollow anode. The geometric model of the gun that is used in these calculations is shown in Fig. 23. The washer shown is an electrode with potential equal to one-half the anode voltage. Focusing solenoids are placed outside the anode, and a "bucking" coil (not shown) is located back of the cathode to reduce the axial magnetic field on the cathode surface to a minimum. Particle trajectories in the gun design were followed a distance of about 2 m from the cathode. The calculations end 60 cm from the cathode. The finite grid structure is not considered.

During actual operation of the gun, both the grid voltage V_g and the anode voltage V_a vary in time over a period of about 50 ns (see section 5.1). The variation of V_a with time approximates one-half of a sine wave,

so that the steady-state conditions simulated with the code are never achieved. In order to gain some insight into the behavior of electrons as V_g and V_a are varied, we make separate calculations with the code for various values of V_g and V_a, thus generating characteristic curves of the gun.

6.3 SIMULATION OF IDEAL OPERATION

In all calculations the current I drawn from the cathode by the extraction grid follows the Child-Langmuir law. For a cathode of area A we have

$$I = 2.3 \times 10^{-6} A V_g^{3/2}/d^2 \ . \tag{3}$$

In this relation V_g is the grid voltage in volts and d is the cathode-grid separation taken to be 1.5 cm in all calculations.

In ideal operation of the gun, the anode voltage is constant in time while the beam current is turned on by applying voltage to the grid. As the grid voltage increases the beam current increases from zero to the desired maximum value. In practice, testing has shown that the anode voltage rises too slowly to achieve this mode of operation with the present gun configuration. Ideal operation is simulated by making separate calculations with the same value of V_a and different values of V_g. Particle trajectories from a 10 inch diameter cathode are displayed in Figs. 24 and 25 for V_a = 2 MV. In these figures the approximately vertical curves are equipotentials and the approximately horizontal curves are particle trajectories. The bell-shaped curve is the axial magnetic focusing field at r = 0. In Fig. 24 we have V_g = 40 kV and I = 4.27 kA, and in Fig. 25 we have V_g = 60 kV and I = 7.82 kA. In these calculations the focusing solenoids are set to provide a maximum axial magnetic field B_z = 520 Gauss on axis at a point about 40 cm from the

cathode as shown in Fig. 21. The trajectories display the focusing from the azimuthal magnetic self-field in the grid-anode region. This focusing force increases with the total current.

6.4 WAVEFORM LIMITED TRANSPORT

The code calculations indicate that under certain circumstances current can be accelerated in the grid-anode region, but not be transported past the peak of the axial magnetic field. This occurs at low anode voltage . This peak value of B_z is set to transport particles with higher energy, and the low energy particles are over-focused. The beam collapses radially and the code results become unreliable because particles are removed from the calculation when their axial velocity becomes negative. Figure 26 shows the calculated beam envelope for various anode voltages. The maximum B_z on axis is 520 Gauss, and the beam current values are chosen just below the limiting current for virtual cathode formation. At $V_a \leq 1$ mV the beam collapses downstream from the peak magnetic field, while for $V_a = 1.5$ MV all of the current is transported.

Experimentally this phenomenon can easily be seen by changing the strength of only the first gun focus coil and observing the current pulse at the gun output. Figure 27 shows experimental results obtained on December 5, 1979, when a 10 inch diameter cathode was used. As shown in Fig. 27a the system timing was such that the current pulse emitted from the cathode was delayed by approximately 20 nanoseconds with respect to the anode voltage pulse. As a result, particles in the leading edge of the current pulse had more energy than those in the trailing edge. Figure 27b shows oscillograms of the gun output current as the current in the gun focus coil was varied. Transmission of the low energy particles in the trailing edge of the current pulse is improved by

lowering the current in the coil, while transmission of the relatively high energy particles in the leading edge and central portion of the current pulse is degraded. The dotted envelope of these oscillograms is the current pulse emitted from the cathode, and represents the maximum current that could be expected at the gun output. Our usual procedure is to "tune" the transport for maximum peak current. This procedure results in the selection of a waveform such as that labled "0".

These oscillograms also illustrate two other phenomena that deserve comment. First, the pulse width of the beam current injected into the accelerator is determined by the relative timing of the cathode current and anode voltage as well as by the waveforms of these pulses. In general this timing depends on many factors in the operation of the system, and as a result the timing adjustment has been difficult to optimize (a continuously variable delay time has been constructed and installed to improve this situation). Second, as the field produced by the first focus coil is adjusted higher than optimum, the pulse width narrows further and the peak amplitude decreases. As shown by the code, this causes the beam to be overfocused producing a virtual cathode at the first waste.

6.5 VIRTUAL CATHODE FORMATION

The formation of a virtual cathode limits the maximum current that can be accelerated by the gun. The current drawn from the cathode by the grid enters the grid-anode region and is accelerated if the anode voltage is sufficiently high. If the anode voltage is not sufficiently high, the results of the calculations show that a virtual cathode forms near the axis a few cm downstream from the grid. The code is not capable of calculations beyond this point. The limiting current that can be accelerated is very nearly a linear function of V_a. It is shown to be linear in the artist's rendition in

Fig. 28 for various diameter cathodes, but the actual theoretical curves drop slightly below the lines at higher values of V_a, as shown in Fig. 30 for a 10 in. diameter cathode. All experimental results discussed in this section were obtained with a 10 in. diameter cathode.

For each value of the limiting current shown in Fig 28 there is a corresponding value of V_g found from Eq. (3). In Fig. 29 the value of V_g required to extract the limiting current is plotted vs V_a. Values of V_g above a given curve result in virtual cathode formation. Calculations indicate that the value of V_g is critical, and a variation of 1 kV in V_g is sufficient to cross from a region of good beam production (below the curve) to virtual cathode formation (above the curve).

It is not surprising that the maximum current that can be accelerated does not obey the relativistic Child-Langmuir law for a one dimensional diode in the grid-anode region[12]. The grid-anode spacing is less than the diameter of the anode. The equipotential surfaces are complicated and change significantly as the current changes, so that the configuration of accelerating electric field bears scant resemblance to a planar diode.

Experiments with a 10 in. diameter cathode show that there is a definite difference in the beam behavior between operating above or below the limiting grid voltage. In the calculations, the code will not run once a virtual cathode is formed. In the experiment, current is indeed accelerated and some of it is transported to the end of the gun (about 2.5 m from the cathode). However, the transported current decreases drastically in the full 10 m of the ETA accelerator. When operating below the limiting grid voltage, the fraction of the cathode current transported to the end of the accelerator is high. These results are shown in Figs. 30 and 31. Figure 30 shows values of cathode current vs V_a for eight experiments. Three data points represent cathode current above the theoretical limiting current, and five data points represent

cathode current below the theoretical limiting current. Figure 31 shows the beam current measured at the cathode and various positions along the entire accelerator for the experimental parameters shown in Fig. 30. When the cathode current lies above the limiting current in Fig. 30, only one-fourth to one-third of the current extracted from the cathode reaches the current monitor 6 m from the cathode. When the cathode current lies below the limiting current in Fig. 30, at least three-fourths of the cathode current reaches the end of the machine.

A possible explanation of these results is that indeed a virtual cathode does form down stream from the grid, but the virtual cathode can act as a source of electrons. No calculations can be performed with the EBQ code in the regime of virtual cathode formation, but it is known that plasma oscillations occur in a virtual cathode. Particles can be emitted with large random velocities so that any beam accelerated from a virtual cathode would have poor quality (i.e., the emittance is high) and be impossible to transport efficiently. The virtual cathode forms in a small region near the axis, but the time dependent electric field generated in this region extends over the entire beam cross-section, distorting the trajectories of particles outside the region. Thus the emittance of the entire beam is increased to the point that only a small fraction of the particles emitted from the cathode are transported to the end of the accelerator.

6.6 BEAM TRANSPORT THROUGH THE ACCELERATOR

In the design of the beam transport for the rest of ETA, the EBQ code was employed primarily to verify analytic calculations and calculations made with the computer code TRANSPORT. Some of the design calculations employing TRANSPORT are described in the following section, where the calculations begin 0.25 m from the cathode. Reiser's theory of relativistic laminar flow was quite useful in the analytic work.[13]

The transport system in the accelerator must satisfy three criteria:

1. Maintain a beam radius sufficiently small to permit passage through the 7.4 cm radius beam pipe. The solenoidal magnetic field B in kG, the beam radius a in cm, beam current I in kA, and energy γ are related by the approximate expression

$$Ba = (1.36\ I/\gamma)^{1/2} \tag{4}$$

2. Maintain a beam radius large enough to avoid formation of a virtual cathode. If the pipe radius b is such that $b/a \leq 2$, the limiting current for virtual cathode formation is given approximately by

$$I = \frac{17(\gamma^{2/3} - 1)^{3/2}}{1 + 2\ln(b/a)} . \tag{5}$$

3. Compensate for the image displacement instability.[14] If the width of the accelerator gaps is w and the length of the solenoid between gaps is L, the criterion can be written as

$$Bb = \left[1.36\ \ I\gamma w/L\right]^{1/2} . \tag{6}$$

The second and third criteria conflict somewhat in that the second places a lower limit on a, and thus an upper limit on B, while the third places a lower limit on B. The solution is to satisfy the limiting current criteria and adjust the separation L to satisfy the third criteria. It turned out that the convenient choice of the distance L determined from mechanical considerations was more than sufficient to resolve the conflict.

The philosophy followed in designing the transport system was to keep the beam radius sufficiently large so that the 10 kA beam current was at least a factor of two below the limiting current given by Eq. (5). This criterion is most stringent at the exit of the gun, where a beam radius of about 4 cm was chosen. From that point on, the limiting current increases with energy so that the beam radius can be allowed to decrease gradually to about 2 cm at the end of the accelerator.

It was deemed desirable to have as few gaps as possible in the solenoidal coils that provide the guide field, and that the necessary gaps be as narrow as possible. A typical "tune" used in the code calculations is shown in Fig. 32 where the axial magnetic field on axis is plotted vs. axial distance along the accelerator. Ordinarily in the TRANSPORT calculations an emittance ε = 50 πmrad-cm was assumed at the exit of the gun. The actual value is not known, the TRANSPORT calculations with $\varepsilon \approx 100\ \pi$mrad-cm indicate that the difference does not significantly alter the beam behavior because the coherent electric and magnetic self forces dominate the behavior throughout the accelerator. This is not true if the emittance is significantly larger than 100 πmrad-cm.

6.7 *TRANSPORT CODE CALCULATIONS*

TRANSPORT code was used to model the beam of a 10 kA beam from near the anode plane through the tapered region of the gun and on through the last accelerator unit. The runs start .25 m from the cathode where the major part of the beam has fully accelerated. The EBQ code was used to obtain the input parameters for the beam radius and outer ray slope. It was then assumed that the beam had 100 π-mr-cm emittance. The magnetic field for the TRANSPORT calculations was modeled using 38 solenoid segments that approximately correspond to the actual individual solenoids (longer solenoids are simulated by two sections). The profile of the magnetic field along the beam axis was then chosen to match a "theoretical" magnetic field tune obtained from the solution of the beam envelope equation. The segmented magnetic field tune used in these TRANSPORT calculations is shown in Figure (33).

The results of the TRANSPORT run for this matched tune are shown in Figure (34). The input parameters are a 10 kA beam injected at 2.5 MeV in an 8.4 cm radius beam at .25 m. The emittance is 100 πmr-cm. Each accelerator

unit then boosts the beam energy by 250 kV. The final accelerator unit is located 10.65 meters from the cathode where the code runs were terminated. As can be seen, the match is quite good with only minor oscillations in the early part of the accelerator. The beam radius is slowly compressed down the transport system to about 2.2 cm at the output.

6.8 TRANSPORT STUDIES OF WAVEFORM LIMITING

Since operation of the accelerator began in May, 1979, many calculations have been made in which both the current and energy were varied. The input current was varied and two code runs were made at 7.5 kA input and 12.5 kA input. These are shown in figure 35 in a composite plot with the matched 10 kA run. This shows that the match does vary with current, but a single magnetic tune can easily handle a current variation of 7.5 kA to 12.5 kA at 2.5 MeV.

The voltage input from the gun was also varied for this same magnetic tune. Input voltages of 2.0, 2.25, 2.5, 2.75 and 3 megavolts are shown in figure 36. Note that at 2.0 MeV the beam hits the wall at the first cyclotron oscillation just beyond the end of the gun taper. At 3 MeV the beam does not hit the wall but is precariously close. Although the wall is shown in the plots, TRANSPORT does not include any effects of the wall interception.

It can be deduced from these code runs that the acceptance of the gun taper and accelerator region of ETA is fairly broad. However, the early and late part of the beam where the energy is low would not transport through the accelerator when the solenoid magnets were tuned for the peak energy.

The most difficult region through which to transport the beam is from the end of the taper in the gun through the first two units of the accelerator.

Here the peaks of the betatron oscillations tend to be the highest. This is the area where experiments have indicated the largest loss of beam.

Oscillograms of beam waveforms are presented in Fig. 37. Notice that the current pulses are approximately one half as wide as the voltage pulse applied to the gun. This results from the waveform limiting discussed above.

7. PROBLEM AREAS AND STATUS

During our tests of the ETA several problems arose that required modifications to parts of the accelerator. These are described in this Section.

7.1 ETA TRIGGER CABLES

The ETA, 250 kV Blumlein sparkgaps are triggered by short duration high-voltage pulses. To distribute the HV pulses, cables are required. Commercial 90 KVDC cable assemblies were purchased as a 125 kV pulse capability was thought to be adequate. The two original units operated in the prototype experiment without trouble.

Operation on the ETA machine revealed that due to shorter trigger pulse duration, higher trigger voltages are required . (The ETA trigger pulses are supplied by trigger Blumleins which have less jitter, shorter duration, and faster risetimes than the trigger transformer used on the earlier ETA prototype test stand experiment.) The higher operating voltage led to peak-to-peak voltages that could exceed 280 kV under certain conditions. The type of cables at the connectors began failing. A thorough electrical analysis revealed an HV stress area within the connector.[15] All the cable ends were x-rayed and it was found that the stresses were further enhanced by poor electrical connections and poor quality control during connector fabrication.

The immediate solution was to shield the stress area with an electrostatic shield cap which could be fitted over the receptacle. The cap effectively transfers the HV stress to the dielectric fluids, relaxes to some extent the mechanical requirements of the cable connectors and extends the HV standoff capability of the assemblies by factors of 2.5 to 4 depending on the

dielectric fluid. In addition a modification of the cable end-connector reduces the stress by a factor of 10 to 20 (within the cable tip) in conjunction with the corona cap. These modifications are incorporated by the supplier in all new and rebuilt cable assemblies.

Other system changes include the addition of a series attenuator at the output of all trigger Blumleins which limits the cable voltage levels and damps transients from the trigger cables. The present operating levels are -80 kV drive with voltage doubling to -160 kV at the sparkgap (effectively an open-circuit).

To satisfy our needs for quality and to monitor the possible causes of failure, each cable end is x-rayed with two orthogonal side views being taken. This applies to all existing cables as well as newly received cables. The supplier is also complying with the design changes and quality control procedures we recommend.

While cable failures have not ceased completely, the incidence of failure has been enhanced considerably. Many of the subsequent failures have been due to improper operating procedures.

7.7 COMPENSATION LOAD RESISTORS

The compensation load resistors initially used in the ETA were type "AS" carborundum resistors. The resistors were selected on the basis of their peak energy and average power ratings: 20,000 joules and 75 watts at 40° ambient. The subsequent testing in the ETA prototype test stand did not reveal any failure modes. However, the Carborundum resistors began failing in the ETA after approximately 30,000-5 ,000 pulses. Examination of the failing resistors showed two major effects. The first is a spalling or flaking of

small chips off the resistor surface. The second effect was an erosion at the interface of the current contact and the body of the resistor. Both effects can eventually lead to catastrophic failure resulting in resistor debri and arcing through the liquid dielectric.

The spalling has been explained[17] as being due to a thermal shock wave generated by the short HV pulse. Although the resistors only absorb about 100 joules in 100 ns, the resulting radial shock wave drives the resistor material first into compression, and then into tension, creating surface stresses which may approach 1000 pounds per square inch and result in material flaking at the resistor-dielectric interface. To reduce the peak tension, an intermediate material between the resistor and dielectric such as a heat conducting epoxy bonded to the resistor was proposed.

The carborundum representatives have provided information on the other failure mode. The erosion between the current contact and the resistor body is due to high current densities at that junction. For pulse applications carborundum now recommends a maximum peak current not to exceed 1 kA per resistor.

When the resistor failures began, other types of resistors were examined. The 1-watt Allen-Bradley carbon resistors chosen to replace the carborundum resistors were selected on the basis of their power handling capability and reliability. Using carbon resistors requires a significant number of resistors in series to maintain reasonable values of voltage and power dissipation. The resistance values needed for the compensation loads (36 in the injector; 58 in the accelerator) also require carbon resistors in parallel. The resulting load consists of printed circuit board packages in series, each package having 15 resistors in series, 8 resistors in parallel and capable of holding 50 kV. With a Blumlein output of 250 kV, the maximum voltage and energy seen by any single carbon resistor in the compensation load is 3.3 kV and 0.28 joules per pulse.

Before the compensation resistor packages were built and installed, the carbon resistors were given both life and destruction tests. For the life tests a small 1 pps pulser driving two resistors in series delivered 800,000-100 ns pulses at 5 kV/resistor (.64 joules/pulse) without resistor failures and a less than 4% long term resistance change. In addition the Blumlein test stand supplied more than 40,000-350 kV pulses at a 1 pps rate to a series stack of four resistor packages (5.8 kV/resistor and .86 joules/pulse) also without failure.

The purpose of the destruction test was to determine the maximum amount of energy a single resistor can absorb before failure.[18] Both 2-watt and 1-watt carbon resistors were tested even though only 1-watt resistors were available in the values required for the compensation loads. Testing in transformer oil (as per operating conditions) showed that destruction of all values of 2-watt resistors occurred at ~ 80 joules for short pulses. Destruction of 1-watt resistors below 10Ω in value occurred at ~ 10 joules and approached 55 joules for larger values. Of the 30,000 resistors installed in the injector and accelerator compensation cans, 8 resistors have failed (all in a single resistor package).

7.3 GAS SEALS FOR THE SPARK GAP BLOWERS

Over the past year we have had a continuing problem with the shaft seals on the spark gap blower system. Oil from the shaft seals drains into the blower housing and is blown throughout the 12" manifold and spark gaps. To eliminate this problem we contracted with the Crane Packing Company to make parts to convert the fluid in the existing shaft seals from oil to gas. Essentially this conversion consists of replacing the rotating graphite seal with a very similar part which operates with nitrogen gas as the lubricating fluid. One half of the axial springs will be removed to reduce the rubbing

friction and permit the "air bearing" feature to function on the sliding surfaces. Since the shaft seals must be pressurized 10 to 20 psig above the inlet blower pressure and operate with a continuous leakage, consumption of nitrogen gas and the pressurizing and dilution of SF_6 in manifolds had to be considered.

The manufacturer conducted tests on a gas seal (single) for a 4" diameter shaft and found that at 120 psig (130 psig on shaft seal) the worst case leakage was 0.1 scfm inward and 0.3 scfm outward. Therefore the gas consumption for the pair of blower seals and for three blowers is:

$$(0.1 + 0.3) \times 2 \times 3 = 2.4 \text{ scfm}$$

$$= 144 \text{ scf/hour}$$

$$= 1150 \text{ scf/8 hr. day}$$

Since a standard 9 x 52 type K cylinder contains only 226 scf of N_2, we connected our seal gas system to an existing tank trailer which has a capacity of approximately 30,000 scf.

At 100 psig each seal can be expected to leak no more than 0.1 scfm into the system. This causes a dilution of a $SF_6 - N_2$ mix if N_2 is used as the seal gas. The question is how fast?

We estimate the volume of each blower system as 125 ft^3. Thus at 100 psig there are

$125 \times \frac{100}{15} = 800$ scf in each blower system. The dilution time constant is

$$t_d = \frac{800}{.1 \times 2} = 4000 \text{ min} = 67 \text{ hrs.}$$

Thus if the % SF_6 is s, then this decays as $s = s_o e^{-.t/t_d}$. If we can stand a 4 - 8 % mix of SF_6, we must purge and refill every 46 hours of running. Note that if the seal leak rate is proportional to pressure, the above time constant is independent of pressure.

The required ΔP across the blower-shaft seal is 10 to 20 psig. We installed a differential pressure switch to maintain a 15 psig differential. If for some reason the differential falls to 10 psig or below, the blower power will be cut off. To maintain the manifold gas system at a predetermined pressure, an adjustable pressure switch activates a solenoid valve to vent sufficient gas to maintain pressure. The operation of the existing N_2, SF_6 fill and vacuum roughing system is not affected.

7.4 CATHODE DEVELOPMENT

The ETA injector uses a hot oxide cathode as the source of electrons. This is fabricated by spraying a mixture of barium and strontium carbonates onto a 10" diameter nickel button containing a trace of zirconium. The button is surface flashed with iridium[19]. The cathode is then indirectly heated in vacuum by a tungsten filament to near 1200°C to convert the carbonates to oxides. Our development tests showed that these cathodes emit up to 40 amps/cm^2 at temperatures near 900°C for up to 1500 hours. Similar cathodes had been used with the Astron accelerator at a current density of approximately 4 amp/cm^2. This is 20% of that required for ETA.

Up until October 1979 our procedure was to activate the cathodes in a test stand before installing the cathode in the ETA gun. Despite our best efforts, the emission of these cathodes were often seriously degraded when checked in the ETA gun.

Many factors have contributed to the poisoning of these cathodes. These include vacuum system reliability; inadequate pumping near the cathode surface (until April 1979); and possibly an oil leak from accelerator unit #1. In October we began activating the cathodes in the ETA injector and could routinely obtain cathodes that emitted between 60 and 100% of the Child-Langmuir current. This shows that exposing the cathode to air while transferring the cathodes from the test stand to the gun also contributed to the poisoning.

Although we expect hot oxide cathodes to be the source of electron for the ETA beam, we are investigating other possible sources. Cold cathodes of the type developed by Loda[20] are being evaluated in our cathode test stand. We will install one of these cathodes in the ETA gun in the near future. We are also developing a 10" diameter dispenser cathode for evaluation in the cathode test stand.

8. FIGURE CAPTIONS

Figure 1 Sketch of the ETA accelerator

Figure 2 The ETA electron gun

Figure 3 Drawing of an ETA induction unit

Figure 4 Diagram of the pulse power conditioning electronics for the ETA gun

Figure 5 Accelerator power conditioning components

Figure 6 Transformer voltage and current waveforms

Figure 7 Cross section of the resonant transformer

Figure 8 ETA Sparkgap

Figure 9 High frequency capacitor voltage probe

Figure 10 Switching system used for monitoring various ETA voltage pulses

Figure 11 Triggering diagram of the ETA accelerator

Figure 12 100 Pulse distribution in firing time delay at three sparkgap pressures

Figure 13 100 Pulse distribution for single and cascaded blumleins

Figure 14 ETA sparkgap triggering versus trigger amplitude at p = 20 psig N_2, $V_{Blumlein}$ = 70 kV (95% self break)

Figure 15 Simplified model of ETA gun

Figure 16 (a) Blumlein voltage required to produce a 2.5 MeV beam

(b) Risetime improvement due to inductive peaking

Figure 17 (a) Oscillogram of the anode voltage pulse

(b) Computed anode voltage pulse using the experimentally determined relative firing sequence shown

(c) Computed anode voltage pulse assuming all gun gaps fired at t = 0.

Figure 18 Equivalent Circuit of an ETA accelerator

Figure 19 Sketch of expected waveforms of accelerator voltage with beam

Figure 20 Measured wave form of voltage across an accelerating unit

Figure 21 Grid drive circuit

Figure 22 Loading of the grid drive.

Figure 23 Geometry of the ETA gun, equipotential surfaces, and particle trajectories for anode voltage V_a = 2 MV, grid voltage V_g = 10 kV, and current I = 532 A.

Figure 24 Equipotential surface and particle trajectories for V_a = 2 MV, V_g = 40 kV, and I = 4.23 kA.

Figure 25 Equipotential surfaces and particle trajectories for V_a = 2 MV, V_g = 60 kV, and I = 7.75 kA.

Figure 26 Beam envelopes for various values of anode voltage. In these calculations the value of the current is slightly below the limiting current for virtual cathode formation.

Figure 27 (a) Oscillograms of anode voltage and cathode current vs. time.

(b) Oscillograms of beam current vs time at the gun output for five values of the peak axial magnetic field. The dashed curve is the cathode current.

Figure 28 Limiting beam current for virtual cathode formation vs. anode voltage for four cathode diameters.

Figure 29 Limiting grid voltage for virtual cathode formation vs anode voltage for four cathode diameters

Figure 30 Limiting beam current for virtual cathode formation vs anode voltage for a 10 in diameter cathode, and data points indicating several separate experiments.

Figure 31 Beam current measured at the cathode and several positions in the accelerator for the experiments indicated in Fig. 30

Figure 32 Magnetic field profile used in transport calculations

Figure 33 Magnetic field profile input to transport for matching a 10 kA beam at 2.5 MeV into the ETA accelerator

Figure 34 Envelope of a matched 10 kA beam injected into the accelerator at 2.5 MeV

Figure 35 Beam envelopes at 2.5 MeV for 7.5, 10 and 12 kA beams

Figure 36 Beam radius of a 10 kAmp beam extracted at 2.0, 2.25, 2.5, 2.75, and 3 MeV

Figure 37 Various oscillograms showing the grid voltage and cathode current; the gun and accelerator voltage; and the beam current pulse at the gun output, the accelerator center and the accelerator output.

Section A-A

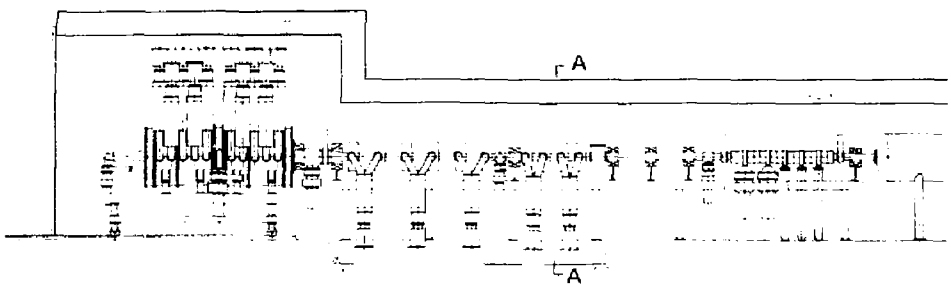

Figure 1

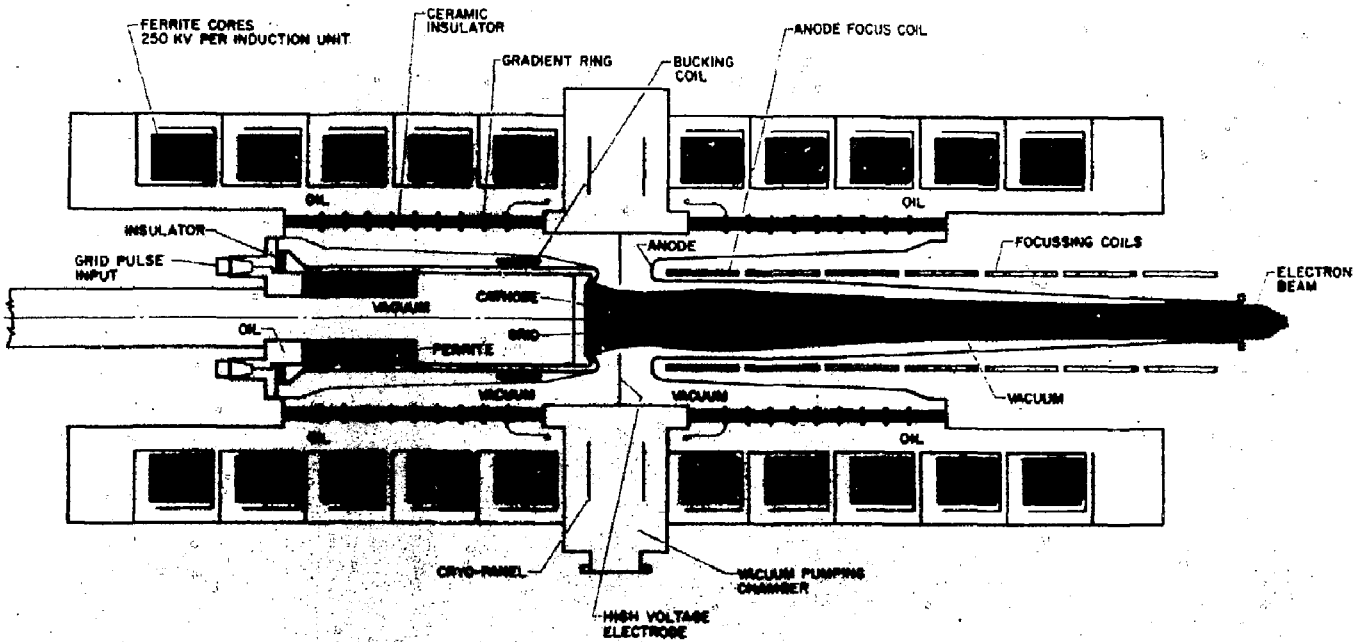

2.5 MEV, 10,000A ELECTRON INJECTOR

Figure 2

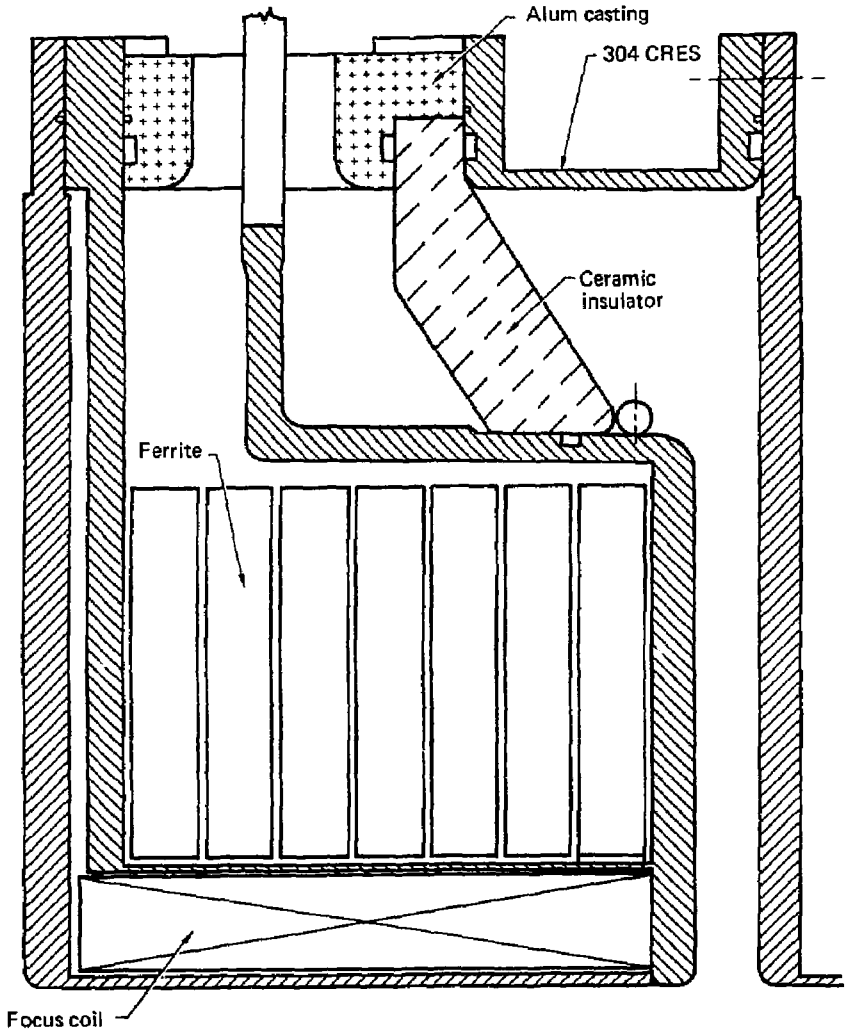
Alum casting
304 CRES
Ceramic insulator
Ferrite
Focus coil
℄

Figure 3

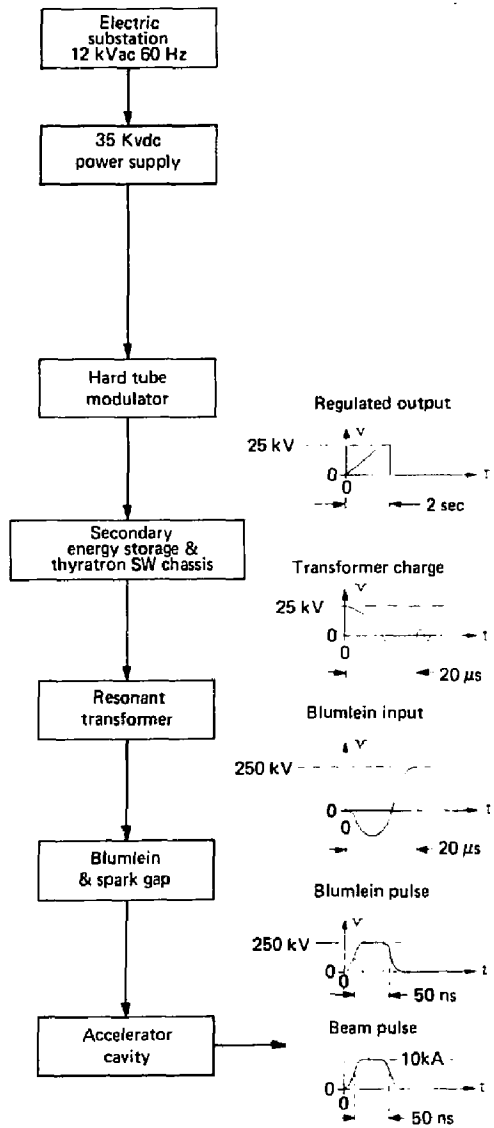
Electric substation 12 kVac 60 Hz
35 Kvdc power supply
Hard tube modulator
Secondary energy storage & thyratron SW chassis
Resonant transformer
Blumlein & spark gap
Accelerator cavity
Regulated output
25 kV
2 sec
Transformer charge
25 kV
20 μs
Blumlein input
250 kV
20 μs
Blumlein pulse
250 kV
50 ns
Beam pulse
10kA
50 ns

Figure 4

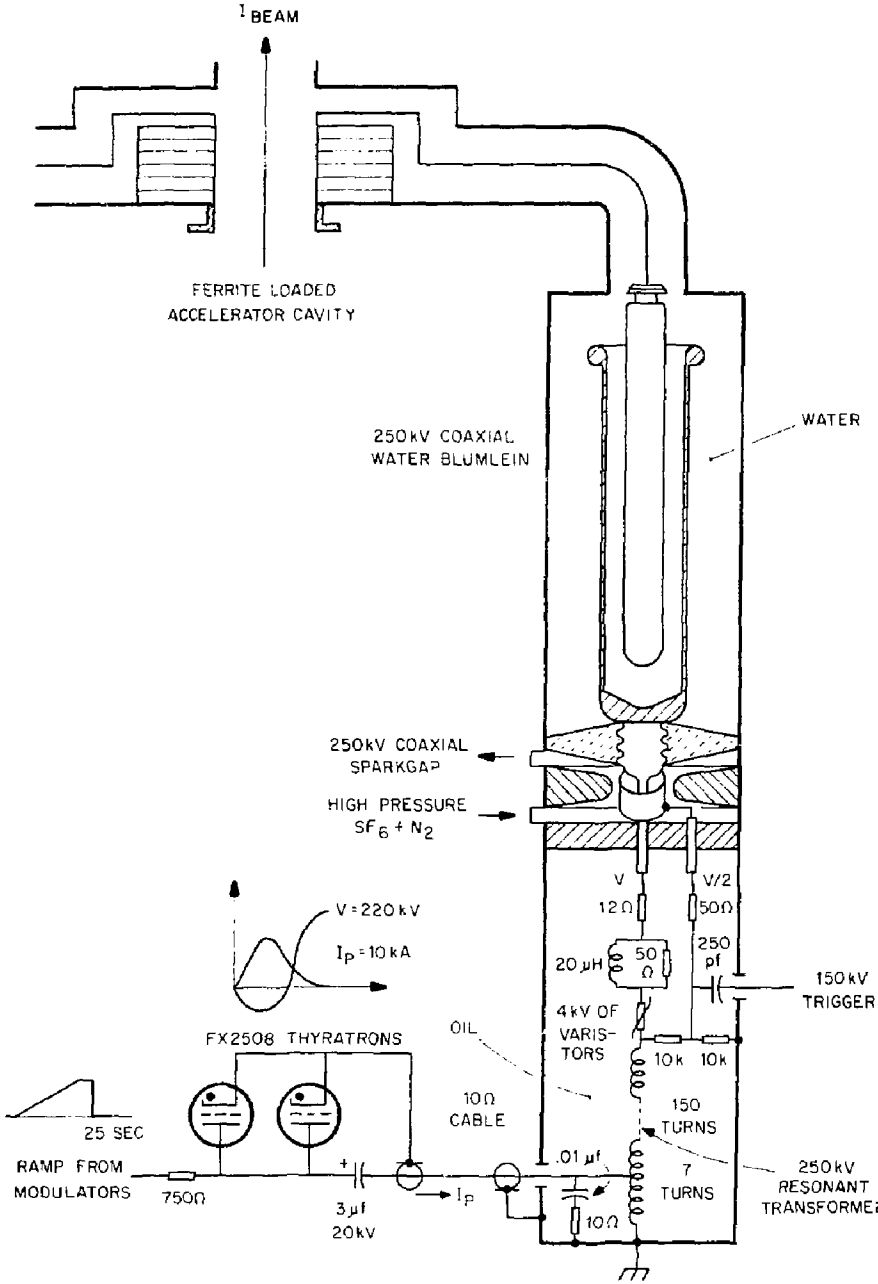
I BEAM
FERRITE LOADED
ACCELERATOR CAVITY
250kV COAXIAL
WATER BLUMLEIN
WATER
250kV COAXIAL
SPARKGAP
HIGH PRESSURE
SF6 + N2
V
V/2
12Ω
50Ω
20 μH
50 Ω
250 pf
150kV
TRIGGER
4kV OF
VARIS-
TORS
10k
10k
OIL
V=220kV
Ip=10kA
FX2508 THYRATRONS
10Ω
CABLE
150
TURNS
25 SEC
RAMP FROM
MODULATORS
750Ω
3μf
20kV
Ip
.01 μf
7
TURNS
250kV
RESONANT
TRANSFORMER
10Ω

Figure 5

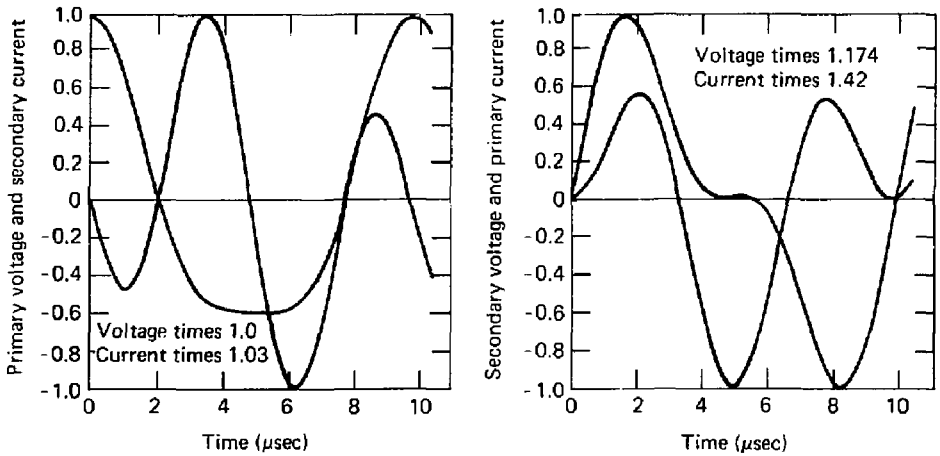
Primary voltage and secondary current
1.0
0.8
0.6
0.4
0.2
0
-0.2
-0.4
-0.6
-0.8
-1.0
0
2
4
6
8
10
Time (μsec)
Voltage times 1.0
Current times 1.03
Secondary voltage and primary current
Voltage times 1.174
Current times 1.42

Figure 6

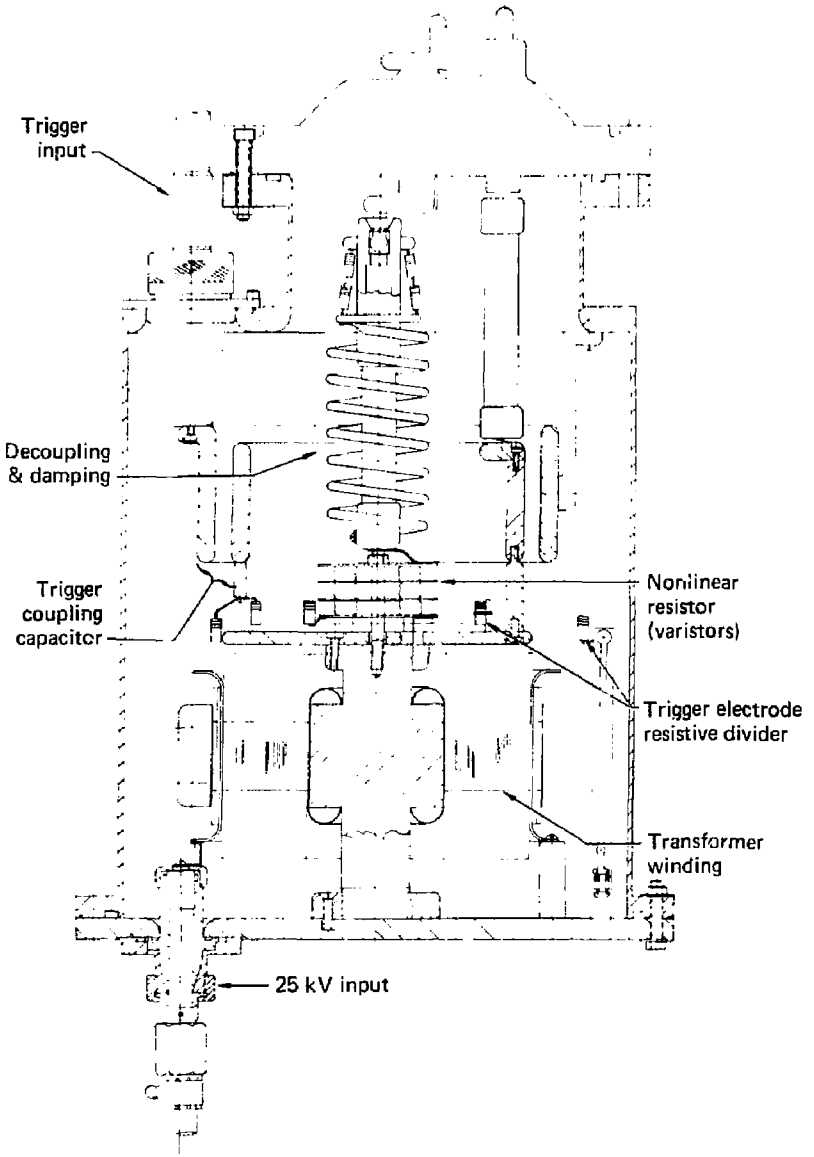
Trigger input
Decoupling & damping
Trigger coupling capacitor
Nonlinear resistor (varistors)
Trigger electrode resistive divider
Transformer winding
25 kV input

Figure 7

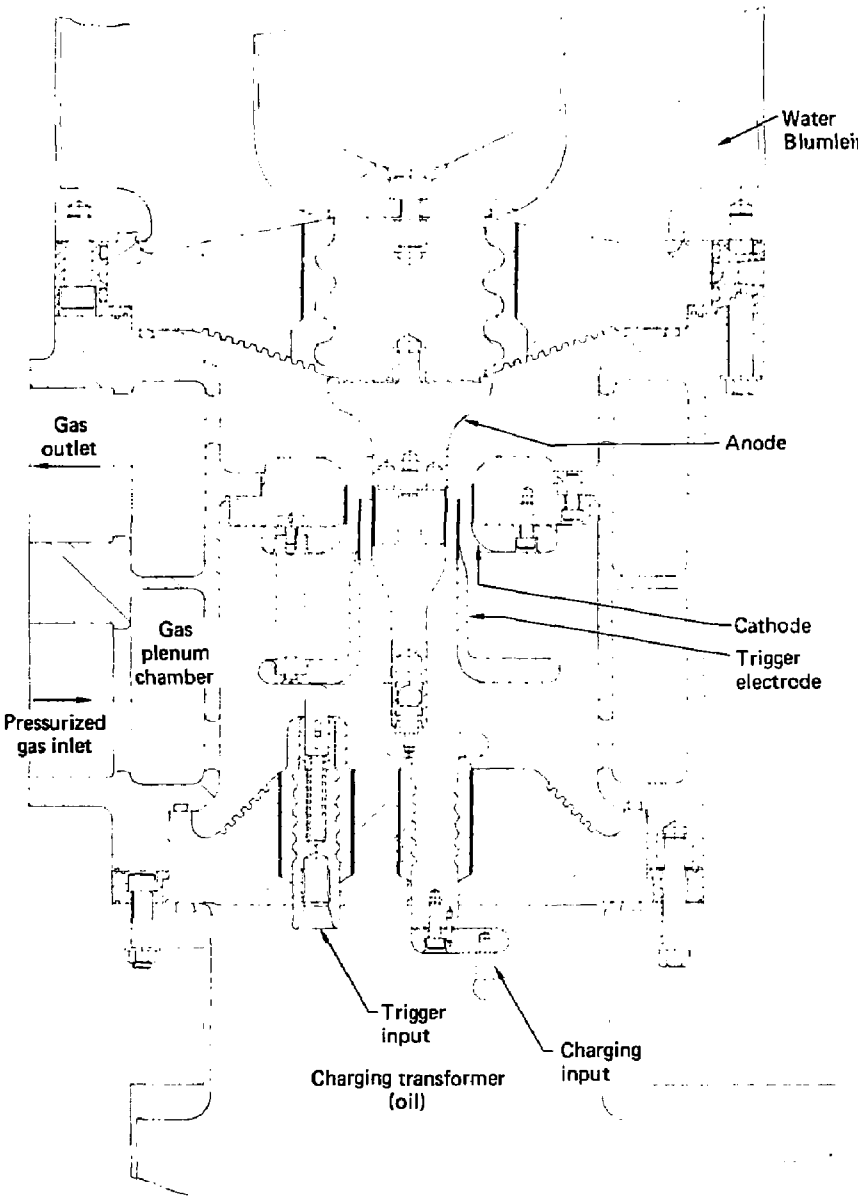
Water
Blumlein
Gas
outlet
Anode
Cathode
Trigger
electrode
Gas
plenum
chamber
Pressurized
gas inlet
Trigger
input
Charging transformer
(oil)
Charging
input

Figure 8

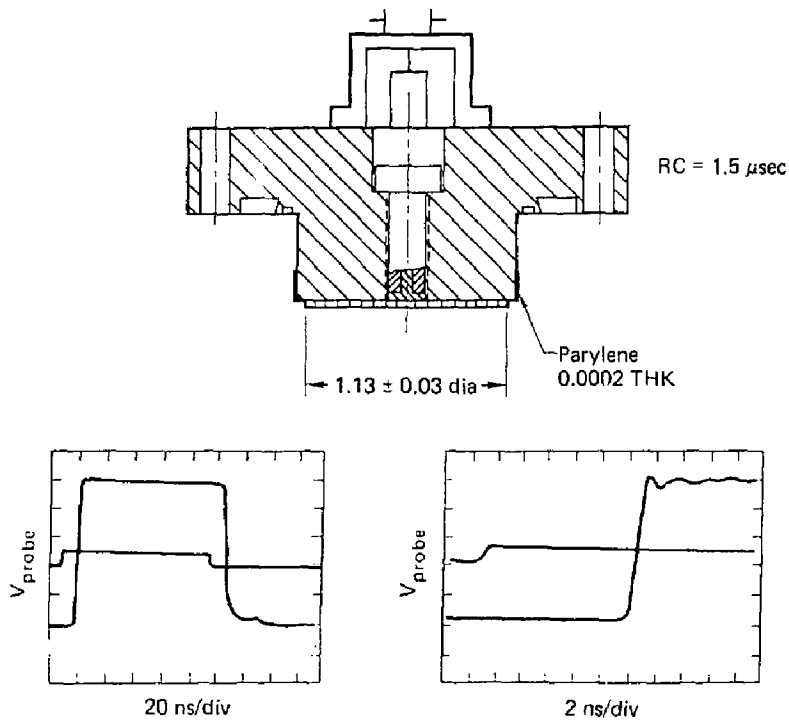
RC = 1.5 μsec
Parylene
0.0002 THK
1.13 ± 0.03 dia
V_{probe}
20 ns/div
V_{probe}
2 ns/div

Figure 9

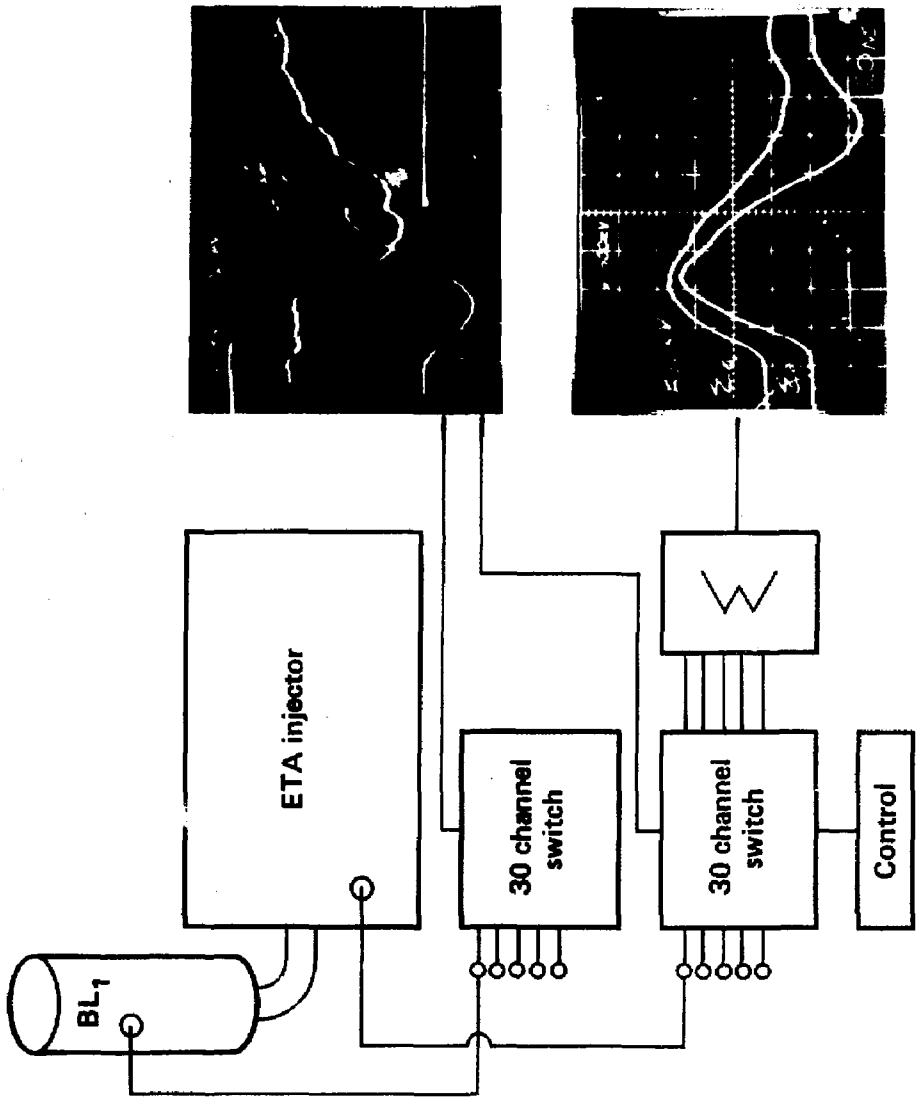
ETA injector
30 channel switch
30 channel switch
Control
BL1

Figure 10

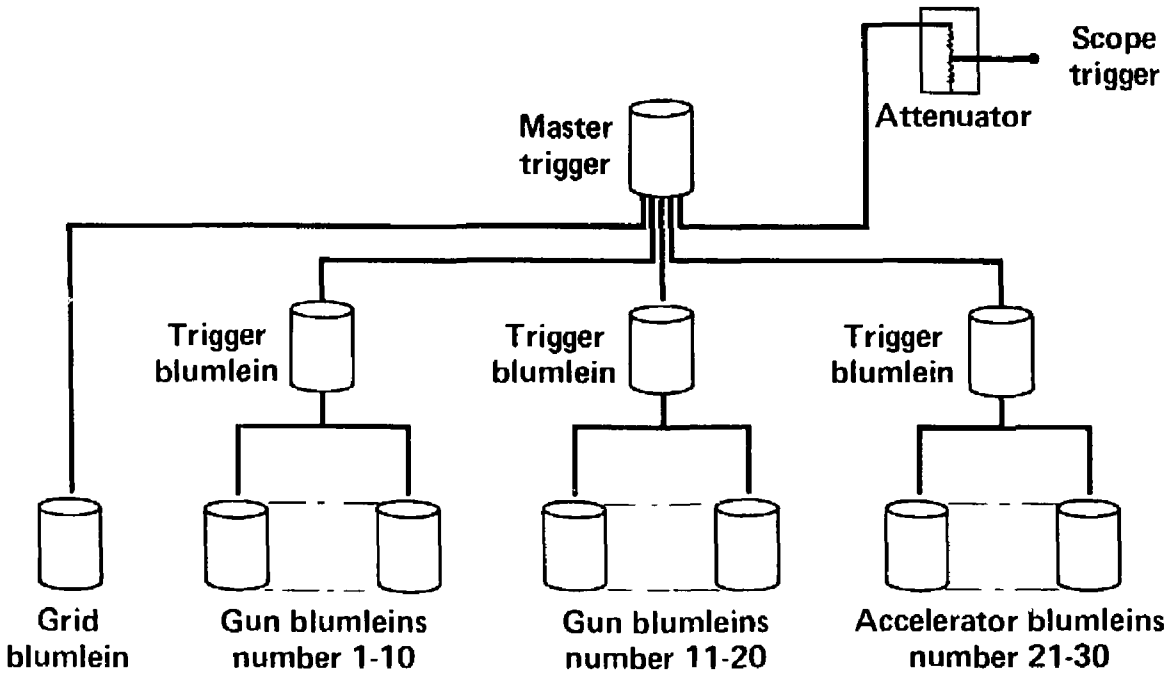
Scope
trigger
Attenuator
Master
trigger
Trigger
blumlein
Trigger
blumlein
Trigger
blumlein
Grid
blumlein
Gun blumleins
number 1-10
Gun blumleins
number 11-20
Accelerator blumleins
number 21-30

Figure 11

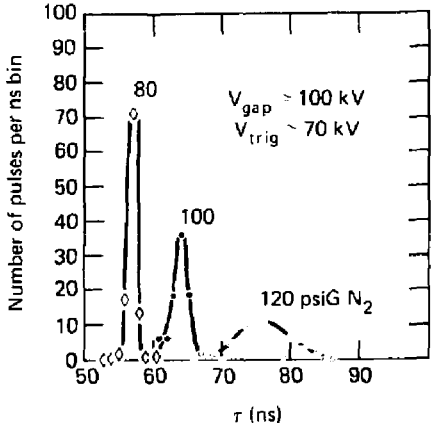
Number of pulses per ns bin
100
90
80
70
60
50
40
30
20
10
0
50
60
70
80
90
τ (ns)
80
100
V_{gap} ≈ 100 kV
V_{trig} ~ 70 kV
120 psiG N_2

Figure 12

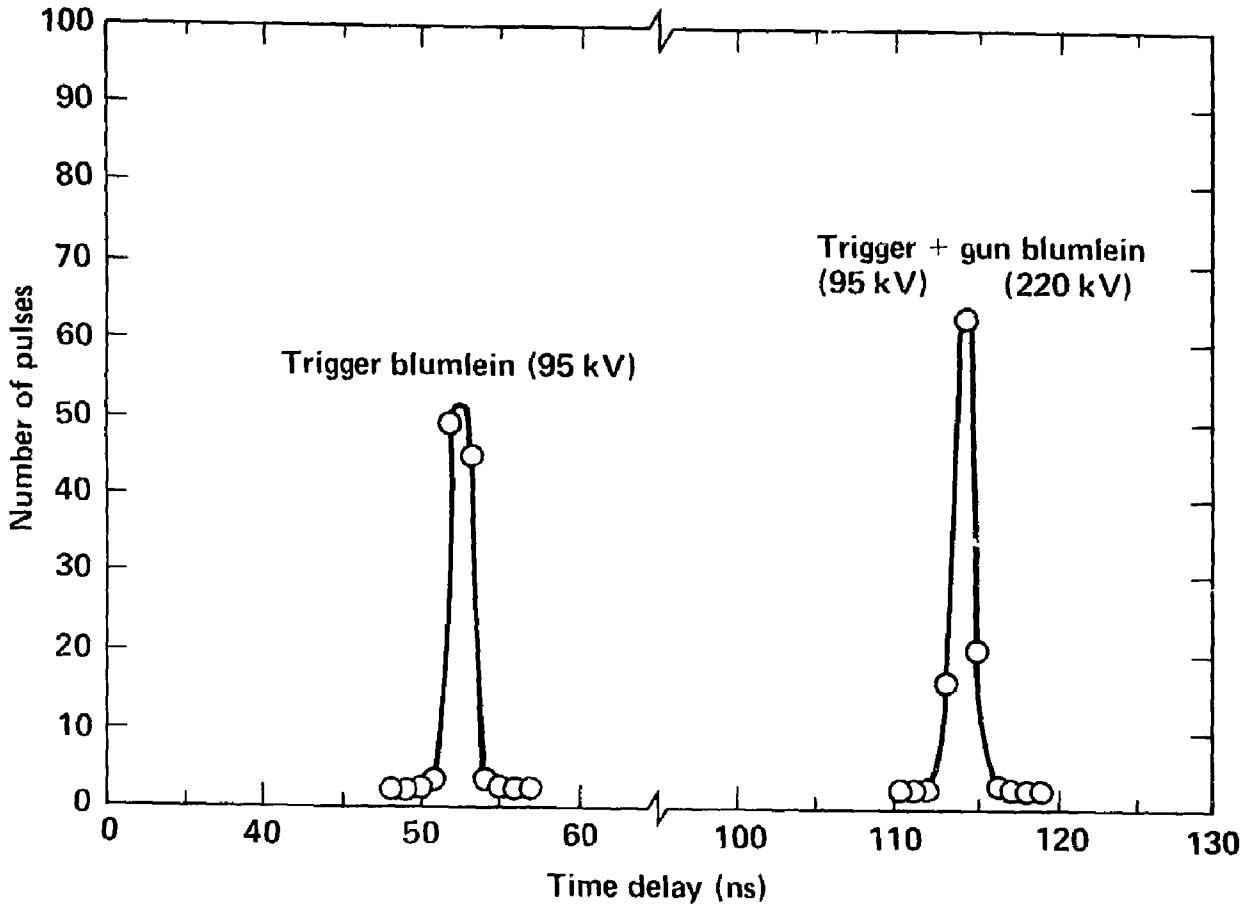
Number of pulses
Time delay (ns)
Trigger blumlein (95 kV)
Trigger + gun blumlein
(95 kV) (220 kV)
0
10
20
30
40
50
60
70
80
90
100
0
40
50
60
100
110
120
130

Figure 13

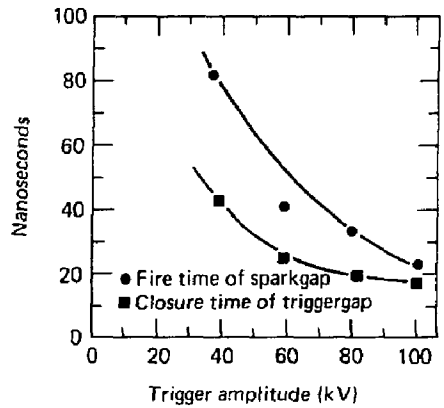
100
80
60
40
20
0
Nanoseconds
● Fire time of sparkgap
■ Closure time of triggergap
0
20
40
60
80
100
Trigger amplitude (kV)

Figure 14

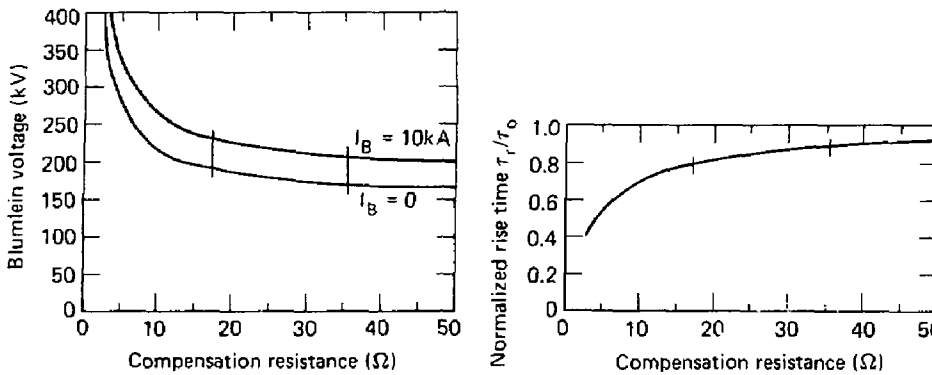
Blumlein voltage (kV)
400
350
300
250
200
150
100
50
0
I_B = 10kA
I_B = 0
0
10
20
30
40
50
Compensation resistance (Ω)
Normalized rise time τ_r/τ_o
1.0
0.8
0.6
0.4
0.2
0
0
10
20
30
40
50
Compensation resistance (Ω)

Figure 16

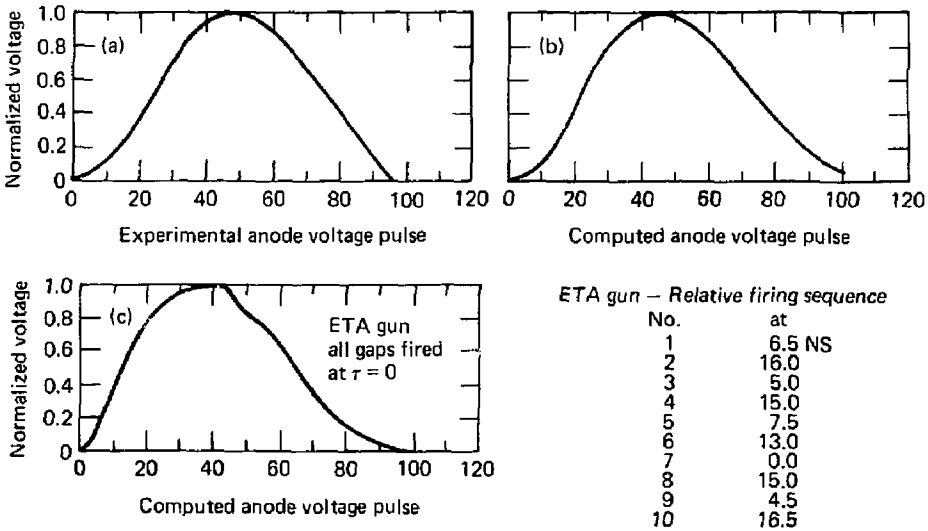

ETA gun — Relative firing sequence

No.	at
1	6.5 NS
2	16.0
3	5.0
4	15.0
5	7.5
6	13.0
7	0.0
8	15.0
9	4.5
10	16.5

Figure 17

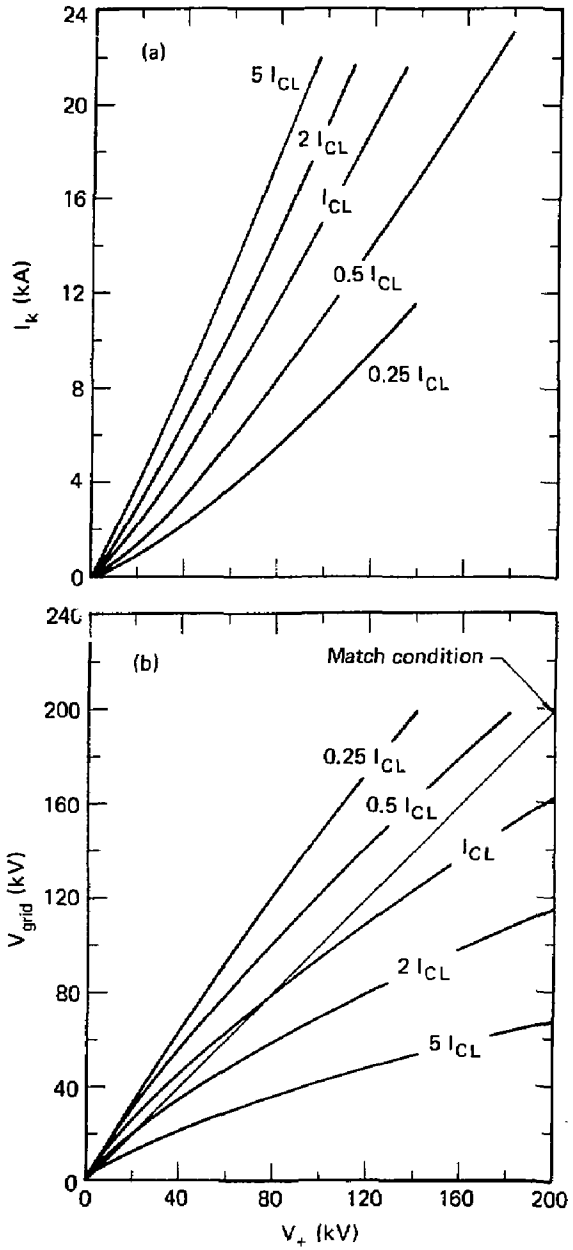
(a)
5 I_{CL}
2 I_{CL}
I_{CL}
0.5 I_{CL}
0.25 I_{CL}
I_k (kA)
0
4
8
12
16
20
24
(b)
Match condition
0.25 I_{CL}
0.5 I_{CL}
I_{CL}
2 I_{CL}
5 I_{CL}
V_{grid} (kV)
0
40
80
120
160
200
240
V_+ (kV)

Figure 22

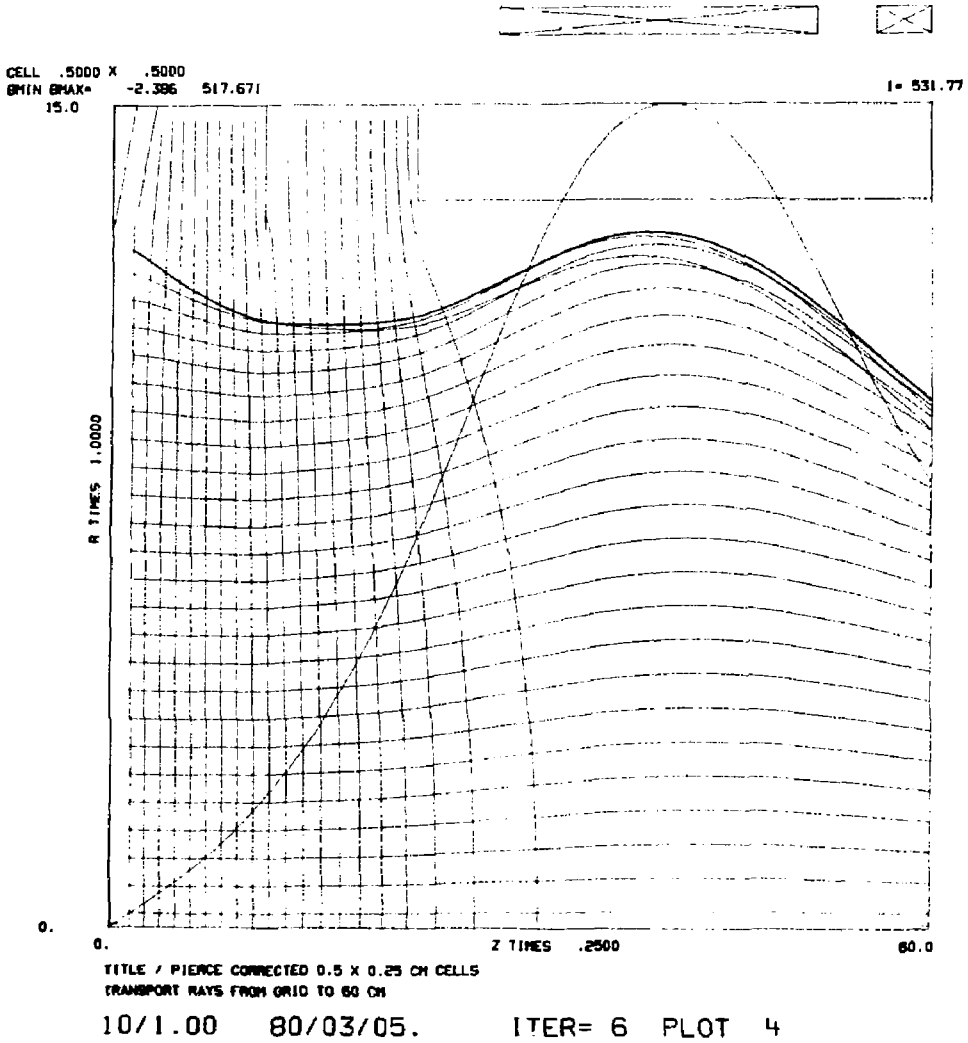
CELL .5000 X .5000
BMIN BMAX= -2.386 517.671
I= 531.77
15.0
R TIMES 1.0000
0.
0.
Z TIMES .2500
60.0
TITLE / PIERCE CORRECTED 0.5 X 0.25 CM CELLS
TRANSPORT RAYS FROM GRID TO 60 CM
10/1.00 80/03/05. ITER= 6 PLOT 4

Figure 23

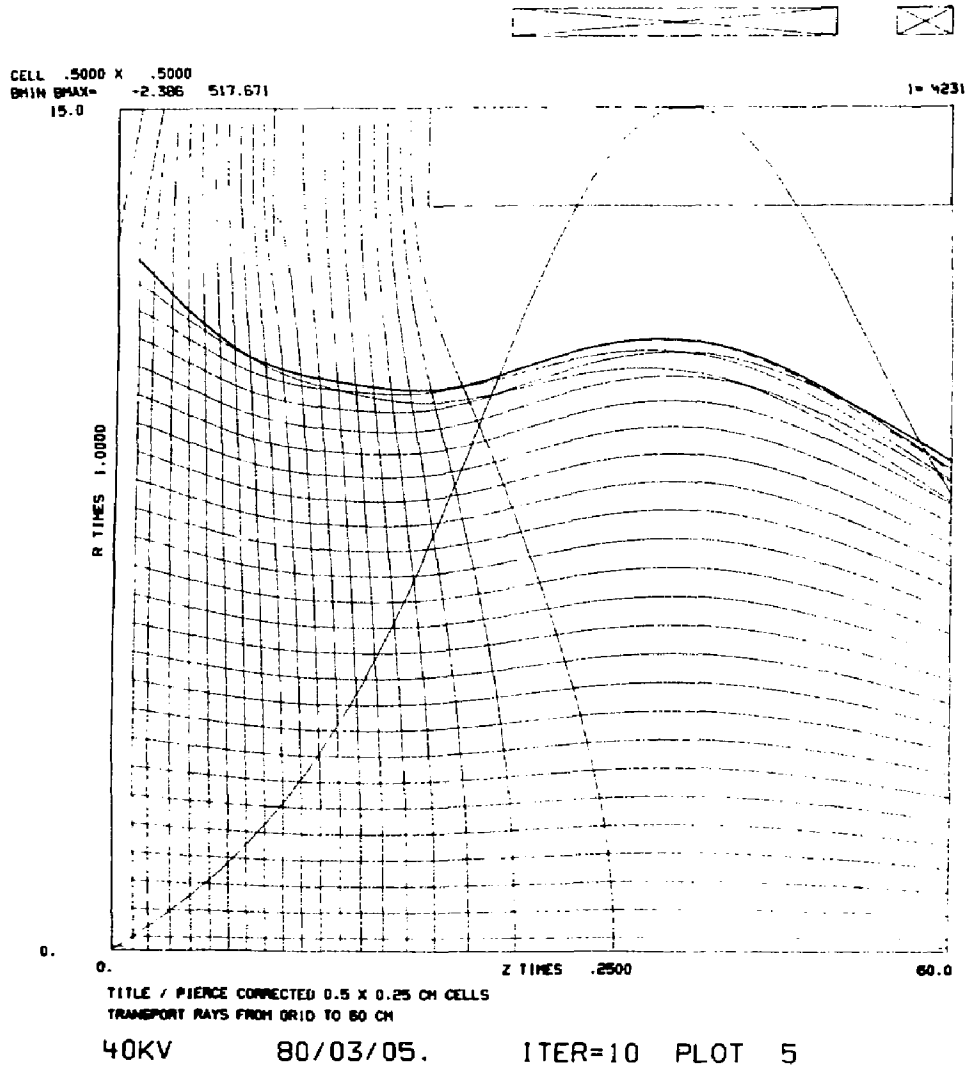
CELL .5000 X .5000
BMIN BMAX= -2.386 517.671
I= 4231.7
15.0
R TIMES 1.0000
0.
0.
Z TIMES .2500
60.0
TITLE / PIERCE CORRECTED 0.5 X 0.25 CM CELLS
TRANSPORT RAYS FROM GRID TO 60 CM
40KV 80/03/05. ITER=10 PLOT 5

Figure 24

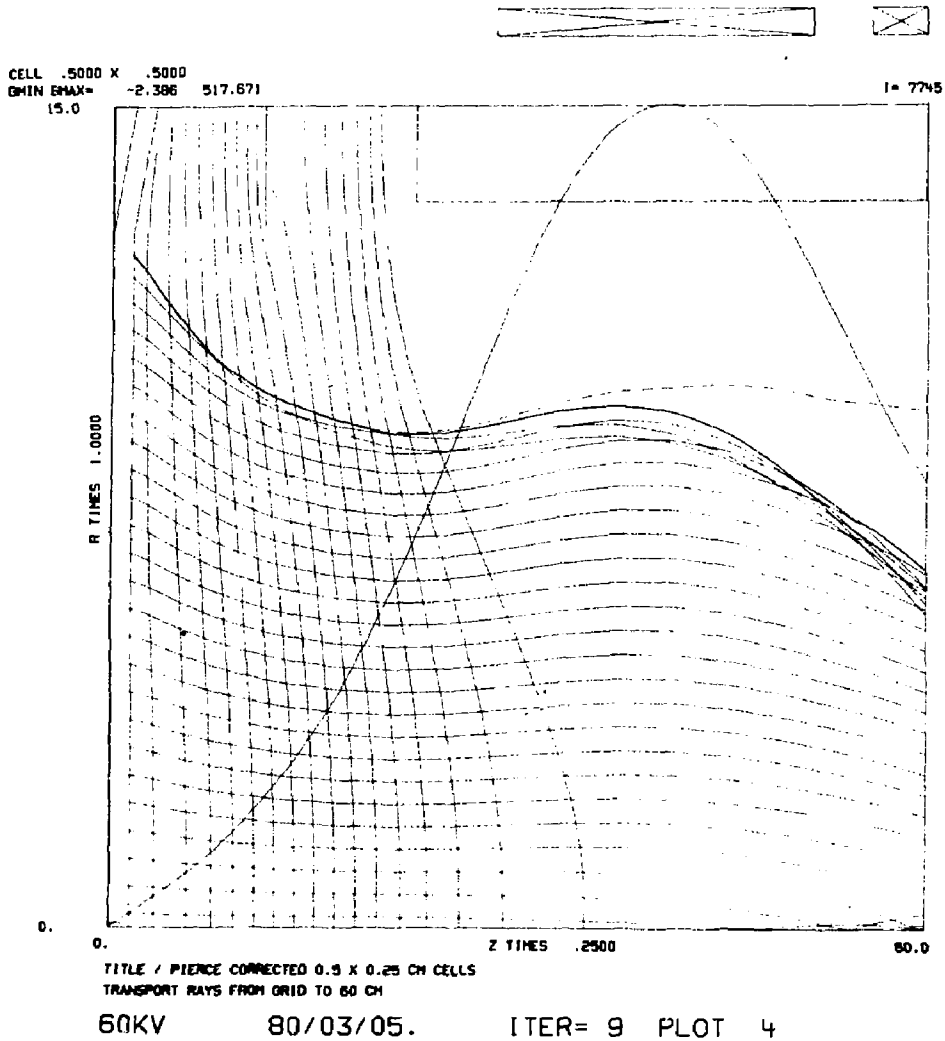
CELL .5000 X .5000
GMIN GMAX= -2.386 517.671
I= 7745.5
15.0
R TIMES 1.0000
0.
0.
Z TIMES .2500
60.0
TITLE / PIERCE CORRECTED 0.9 X 0.25 CM CELLS
TRANSPORT RAYS FROM GRID TO 60 CM
60KV 80/03/05. ITER= 9 PLOT 4

Figure 25

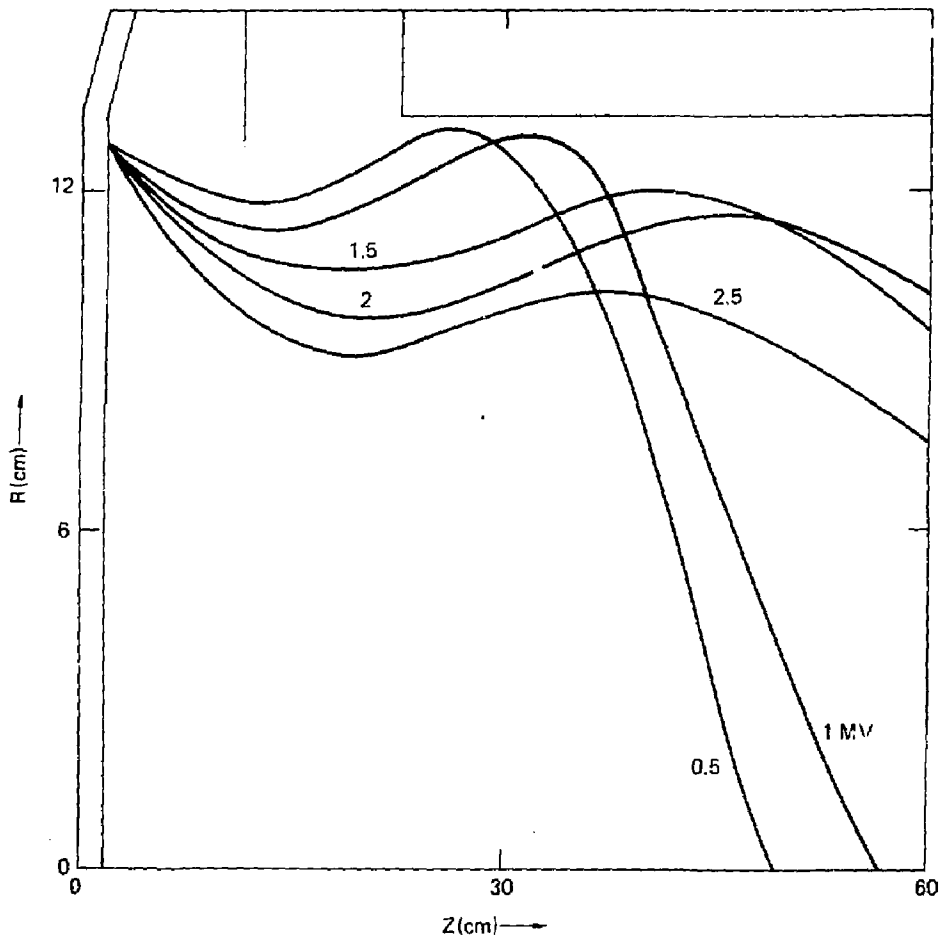

Figure 26

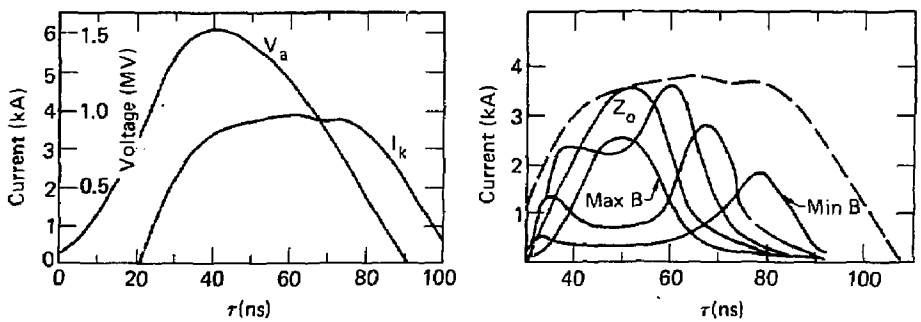
Current (kA)
Voltage (MV)
1.5
1.0
0.5
V_a
I_k
0
20
40
60
80
100
τ(ns)
Current (kA)
Z_o
Max B
Min B
40
60
80
100
τ(ns)

Figure 27

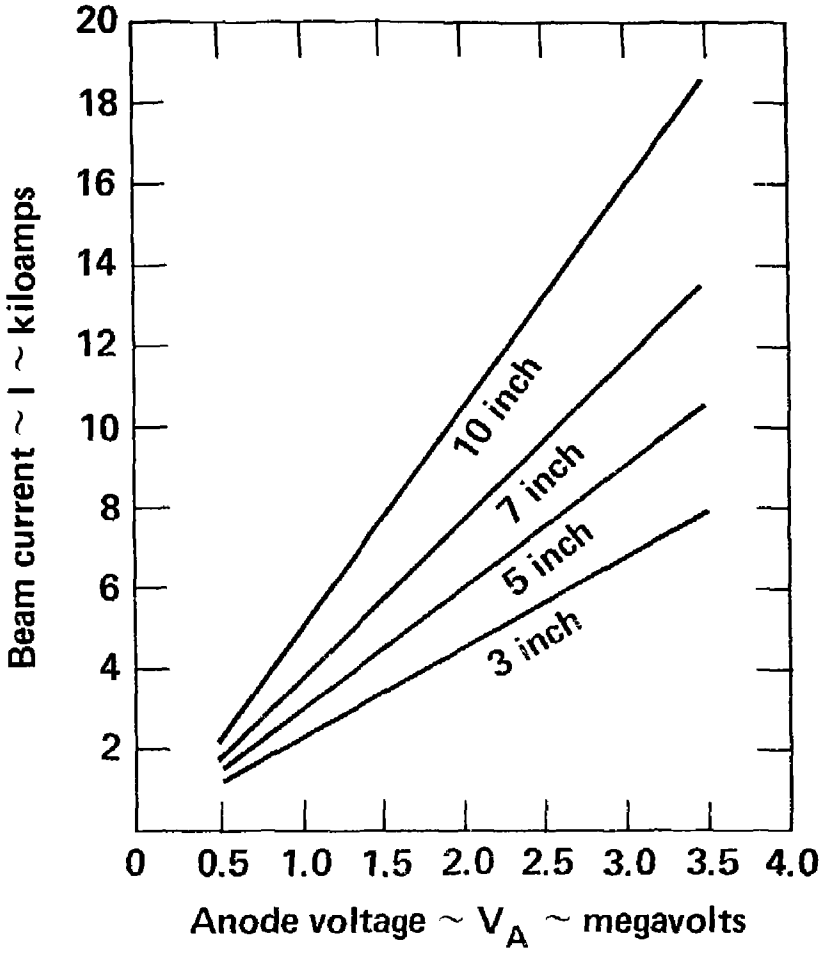
Beam current ~ I ~ kiloamps
20
18
16
14
12
10
8
6
4
2
10 inch
7 inch
5 inch
3 inch
0
0.5
1.0
1.5
2.0
2.5
3.0
3.5
4.0
Anode voltage ~ V_A ~ megavolts

Figure 28

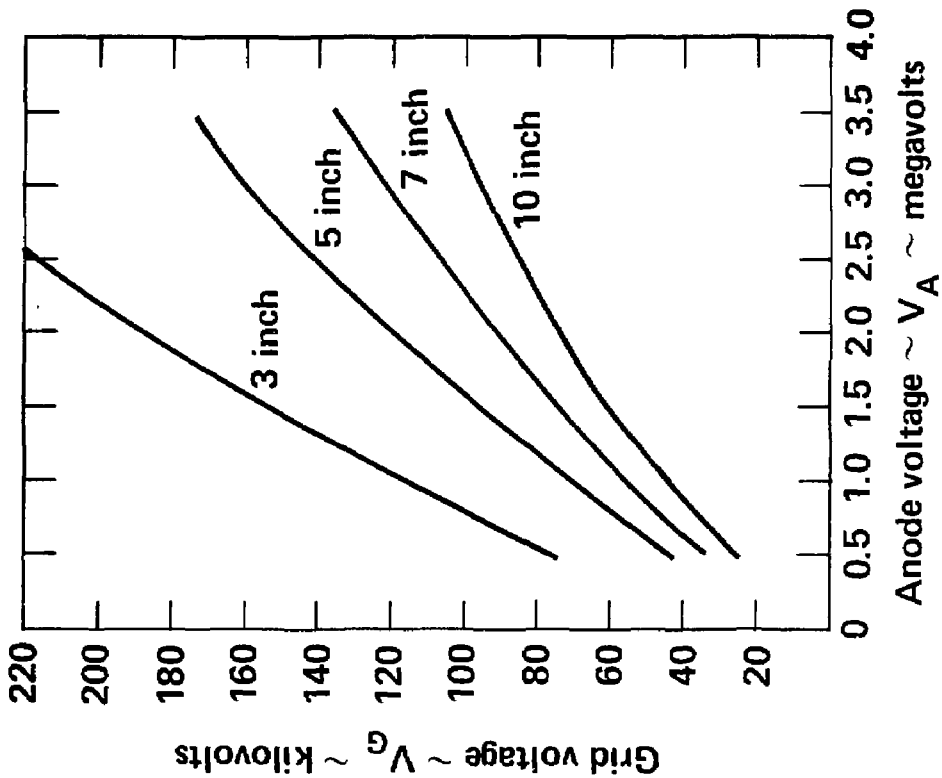
Grid voltage ~ V_G ~ kilovolts
220
200
180
160
140
120
100
80
60
40
20
0
0.5
1.0
1.5
2.0
2.5
3.0
3.5
4.0
Anode voltage ~ V_A ~ megavolts
3 inch
5 inch
7 inch
10 inch

Figure 29

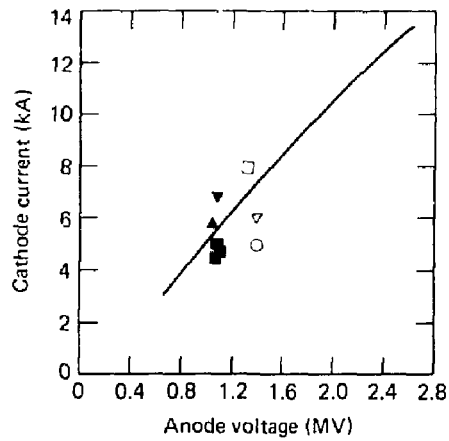
14
12
10
8
6
4
2
0
Cathode current (kA)
0
0.4
0.8
1.2
1.6
2.0
2.4
2.8
Anode voltage (MV)

Figure 30

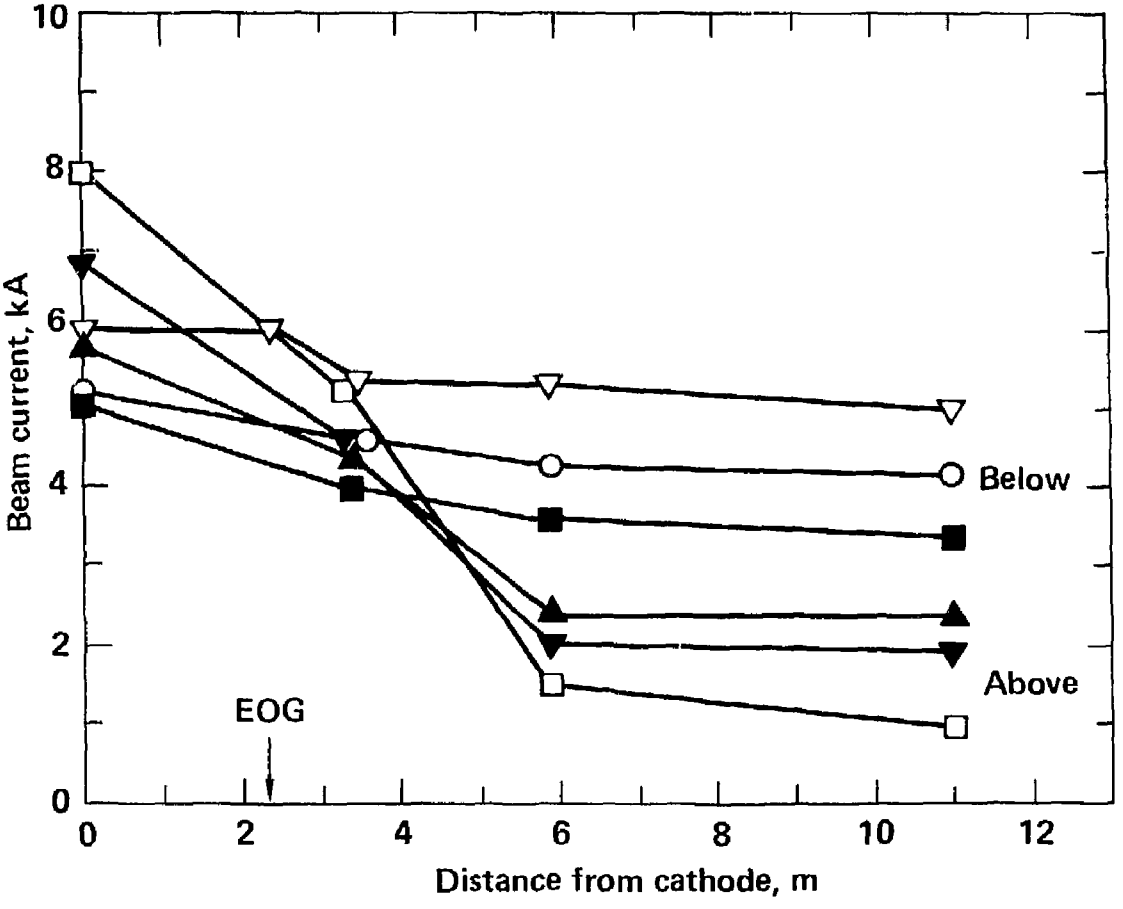
10
8
6
4
2
0
Beam current, kA
0
2
4
6
8
10
12
Distance from cathode, m
EOG
Below
Above

Figure 31

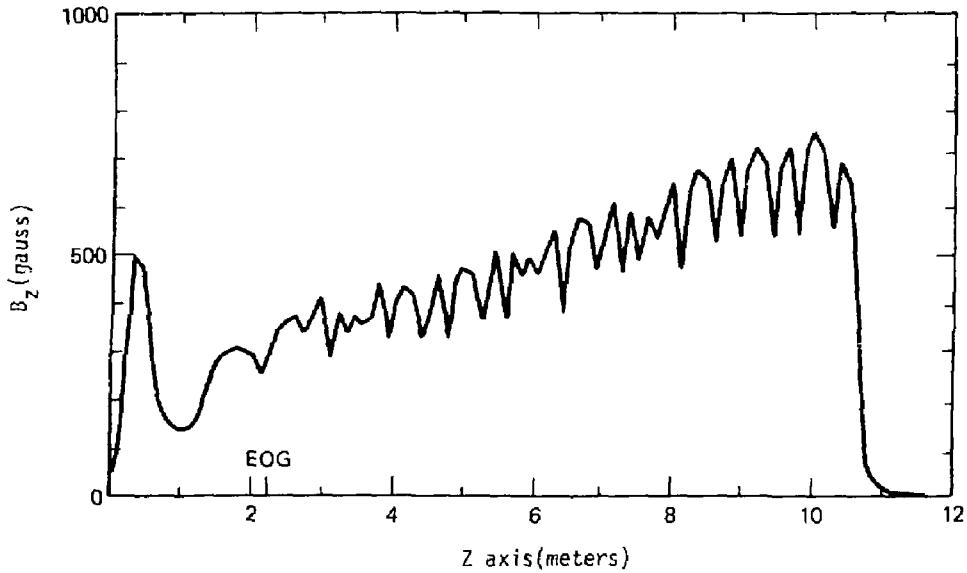

Figure 32

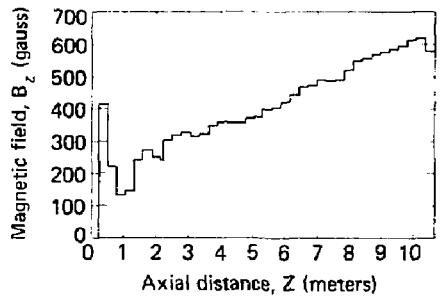
Magnetic field, B_z (gauss)
700
600
500
400
300
200
100
0
0 1 2 3 4 5 6 7 8 9 10
Axial distance, Z (meters)

Figure 33

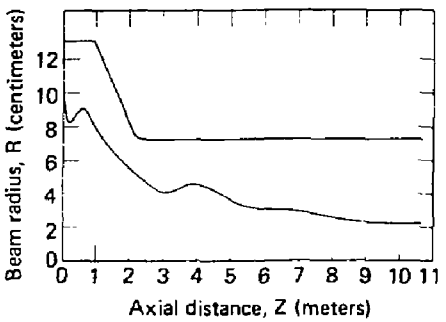
Beam radius, R (centimeters)
12
10
8
6
4
2
0
0 1 2 3 4 5 6 7 8 9 10 11
Axial distance, Z (meters)

Figure 34

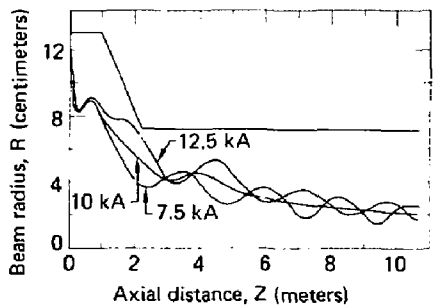
Beam radius, R (centimeters)
12
8
4
0
12.5 kA
10 kA
7.5 kA
0
2
4
6
8
10
Axial distance, Z (meters)

Figure 35

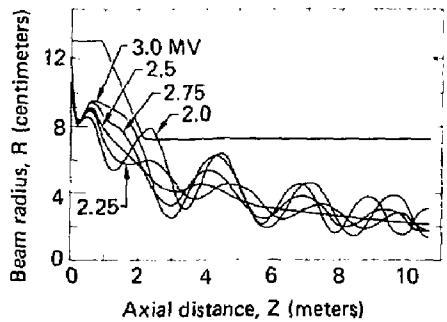
Beam radius, R (centimeters)
12
8
4
0
3.0 MV
2.5
2.75
2.0
2.25
0
2
4
6
8
10
Axial distance, Z (meters)

Figure 36

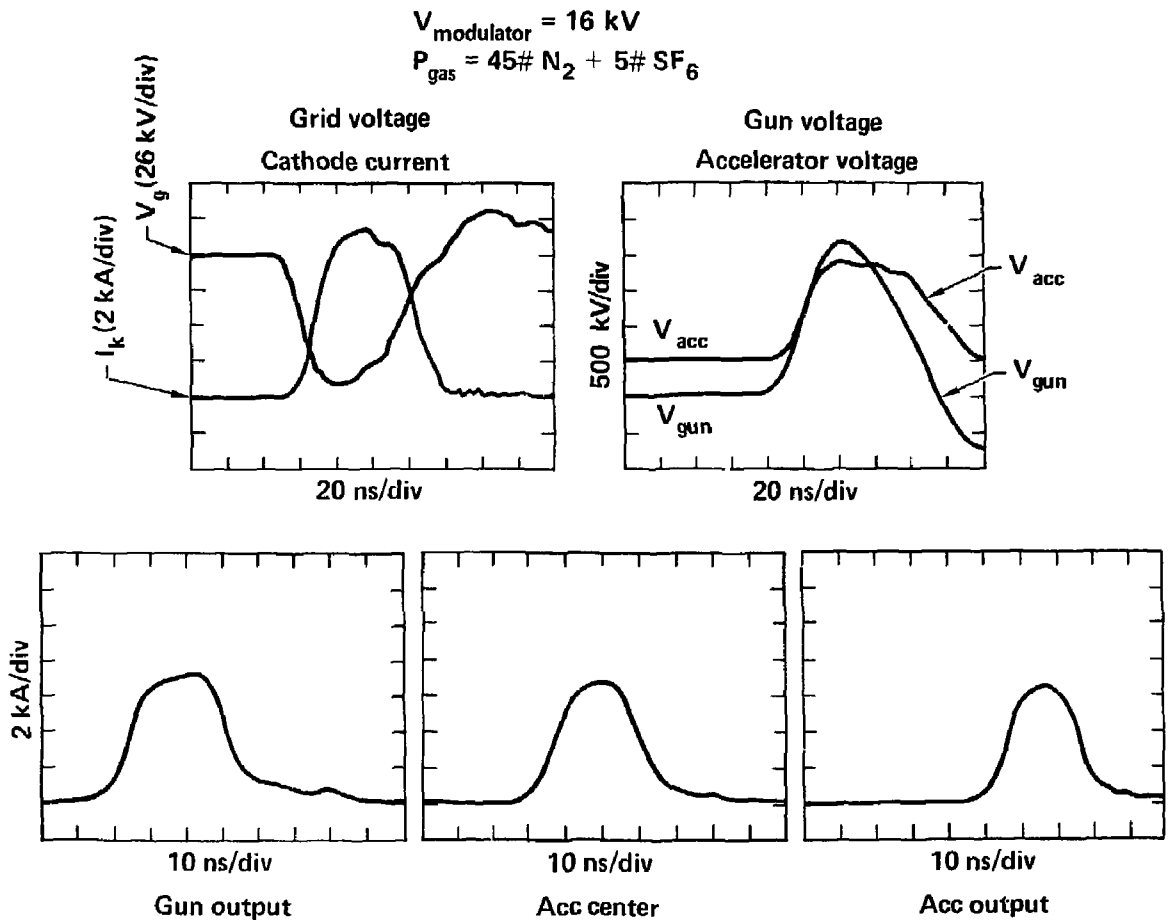
$V_{modulator}$ = 16 kV
P_{gas} = 45# N_2 + 5# SF_6
Grid voltage
Cathode current
V_g (26 kV/div)
I_k (2 kA/div)
20 ns/div
Gun voltage
Accelerator voltage
500 kV/div
V_{acc}
V_{gun}
20 ns/div
2 kA/div
10 ns/div
Gun output
10 ns/div
Acc center
10 ns/div
Acc output

Figure 37

9. REFERENCES

1. N. Christofilos, R. Hester, W. Lamb, D. Reagon, W. Sherwood and R. Wright, "High Current Linear Induction Acce rator for Electrons," Rev. Sci. Instrum. Vol. 35, No. 7, 886-890, July 1964. See Also:

   J. Beal, N. Christofilos, and R. Hester, "The Astron Linear Induction Accelerator," 1969 Particle Accelerator Conference, March 5-6, 1969 (LLNL report UCRL 71405).

2. The ERA 4 MeV Injector Avery etc., 1979 Particle Accelerator Conference, Accelerator Engineering and Technology, March 1-3, 197, IEEE Trans. Nucl. Sci., 18 (1971).

3. A. Faltens, L. Reginato, R. Hester, E. Cook, A. Chesterman, T. Yokota, W. Dexter, "High-Repetition-Rate Burst-Mode Spark Gap," IEEE 1978 Thirteenth Pulse Power Modulator Symposium.

4. E. Cook, L. Reginato, "Off Resonance Transformer Charging for 250-kV Water Blumlein," IEEE 1978 Thirteenth Pulse Power Modulator Symposium.

5. L. Reginato, E. Cook, W. Dexter, J. Schmidt, "Pulsed Ferrite Core Tests for 50-ns Linear Induction Accelerator," Presented at the International Magnetics Conference, Florence, Italy, May 9-12, 1978 (UCRL 80811).

6. R. Hester, D. Bubp, J. Clark, A. Chesterman, E. Cook, W. Dexter, T. Fessenden, L. Reginato, T. Yokota, A. Faltens, "The Experimental Test Accelerator (ETA)," IEEE Trans. Nucl. Scien. NS-26, 3, (1979). p. 4180 (UCRL 82448).

7. T. J. Fessenden, "The Astron On-Line Beam Energy Analyzer," Rev. Sci. Instrum. Vol. 43, No. 8, August 1972

8. E. J. Lauer, "Measurements of Distributions in Firing Time Delay of the ETA Test Spark Gap Switch," Internal Beam Research Program report, ATA Note 64 (1979)

9. R. J. Briggs, "Blumlein Voltage Waveforms," Internal Beam Research Program report, ATA Note 84 (1979).

10 "Electrical Design of Ballast-Termination," Ian Smith (FXR Note 1073)

11. A. C. Paul, V. K. Neil, "Computational Studies of Beam Dynamics in the ETA Gun," IEEE Trans. Nucl. Scien. NS-26, 3, (1979) p. 4242, also Lawrence Berkeley Laboratory report LBL 8409.

12 J. E. Boers and D. Kelleher, J. App. Phys. 40, 6 (1969). See also H. R. Jory and A. W. Trivelpiece, J. App. Phys. 40 10 (1969).

13. M. Reiser, "Laminar-flow Equilibria and Limiting Currents in Magnetically Focused Relativistic Beams," Phys. Fluids, Vol. 20, No. 3, March 1977

14. V. K. Neil, "The Image Displacement Effect in Linear Induction Accelerators" Lawrence Livermore Laboratory Report UCID 17976, Nov. 13, 1978.

15. J. C. Clark, "JASON--Solutions for the Fields in the High Voltage Connector," Internal Beam Research Program report, ATA Note 59 (1979) and J. C. .Clark, "JASON Solutions for Final Cap Configuration to Reduce Breakdown hazard in high voltage Connector," ATA Note 61 (1979).

16. R. Spoerlein, K. Olsen, "High Voltage Cable Connector Problems," Internal Beam Research Program report, ATA Note 73 (1979).

17. A. Faltens, "Failure of the Carborundum Resistors," Internal Beam Research Program report, ATA Note Note 80 (1980).

18. D. Birx, "A Brief Note on the Power Handling Capabilities of Allen Bradley 2-Watt Resistors," Internal Beam Research Program report, ATA Note 101 (1980).

19. H. R. Cavagnolo, "Use of Iridium Substrata to Obtain High Current Densities at Low Operating Temperatures with Conventional Oxide Cathodes," Internal Beam Research Program report, ATA Note 17 (1976).

20. Gary Loda, "Electron Gun for High Average Power UV/Visible Lasers," Systems, Science and Software report SSS-79-1140-FR (January 1979).